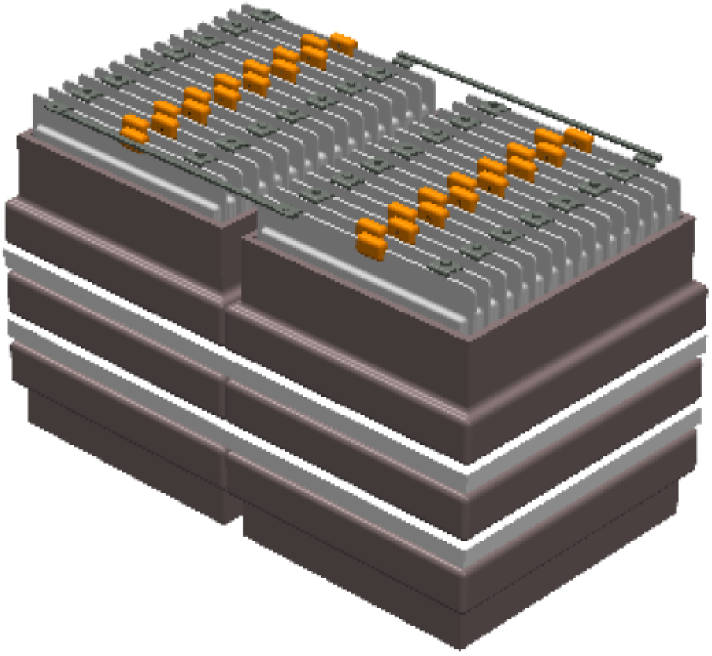

Operando plasmon resonance sensoring applied to sodium-ion batteries

Towards enhancing contemporary measuring systems

Master's thesis in Materials Chemistry

Stefan Ewaldsson

DEPARTMENT OF PHYSICS
CHALMERS UNIVERSITY OF TECHNOLOGY
Gothenburg, Sweden 2022
www.chalmers.se

Master's thesis 2022

Operando plasmon resonance sensoring applied to sodium-ion batteries

Towards enhancing contemporary measuring systems

STEFAN EWALDSSON

Department of Physics
Chalmers University of Technology
Gothenburg, Sweden 2022

Operando plasmon resonance sensoring applied to sodium-ion batteries
Towards enhancing contemporary measuring systems
STEFAN EWALDSSON

Supervisor: Elin Langhammer, Athmane Boulaoued and Christian Sundvall, Insplorion
Examiner: Patrik Johansson, Department of Physics, Chalmers University of Technology

Master's Thesis 2022
Department of Physics
Chalmers University of Technology
SE-412 96 Gothenburg
Telephone +46 31 772 1000

Cover: A battery pack showing how the sensors (in orange) can be mounted and implemented for sending information to the battery control module (BCM).

Typeset in LaTeX
Gothenburg, Sweden 2022

Abstract

The sodium-ion storage mechanism in hard carbon was studied by the means of nano-plasmonic resonance spectroscopy. The measurements were made *operando*, using a gold nano-film deposited onto an optical fiber which was inserted into a battery half cell, cycled at different C-rates. The most favourable sensor type was also investigated. It was found that correlation between the optical signal and voltage signal was possible. The fast cycles in the cycling regime used, led to capacity fade, which can be seen to mainly affect the plateau region of the discharge voltage signal. This could be explained by the more sluggish diffusion of intercalated sodium-ions in the hard carbon structure.

The first cycle of the cells showed a unique response in the optical spectra, suggesting that the fiber is sensitive to events during formation cycles, such as the solid electrolyte interphase formation.

Keywords: Nano-plasmonic sensing, Na-ion, Hard carbon, Na-ion storage mechanism, Fiber optical battery sensing.

Acknowledgements

The task of writing a full year thesis all by myself did not at first seem as tough as it turned out to be in the end. I want to thank Athmane Boulaoued, for creating the project and supervising me through the first phases of the project. Thank you Christian Sundvall, for taking over the role of supervisor after Athmane, and all the time and effort you put into reading my report. A great thanks is also owed to Saima Zaman, for making me the fibers I needed and for teaching me how to handle them.

Thank you Elin Langhammer and Patrik Johansson for the invaluable feedback and insights you gave me during our follow up meetings.

Thanks to Marcus Thim for being my opponent and taking the time to read and prepare for my defense, and in spite of the complicated presentation manage to get a bunch of good questions out there.

During my entire time at Insplorion, I have felt welcome and home. To have a place to work and colleagues to talk to was very welcome after having spent the previous year studying remotely during the pandemic. Being treated like a part of the team was not only heart-warming, but very educational as well as I got to attend various meetings and learn a lot about company structure.

During the time at Chalmers I have had the privilege to meet so many great people from different divisions and in different settings, that I feel like I cannot mention all of you here. Many of you have taught me more valuable lessons than the professors ever could, and I hope that I will share many more memories with you.

Thanks to my family, Birgit, Lars and Ann, for always being there for me, whether I need someone to talk to or just an escape from the hectic life in the city. Thank you for all the love and support!

Last but not least, thank you Ellinor for keeping me together and focused, and for your never ending love and encouragement. I could not have done this without you.

Stefan Ewaldsson, Gothenburg, December 2021

Table of contents

List of Figures

List of Tables

1

Introduction

Sodium-ion batteries (SIBs) have attracted much attention during the past decade as an alternative to lithium-ion batteries (LIBs), especially for large-scale energy storage applications [1]. SIBs are showing a number of significant advantages over LIBs, such as ease of storage and transportation along with having abundant and easily accessible raw materials, thus explaining the attention these systems have received [1–7]. The stochastic nature of some green energy sources such as wind and solar, require us to be able to stabilize the energy to enable us to use it during the times where no energy is produced, during the night or during windless days. This among other applications connected to our ever-growing energy consumption, have highlighted the need for further development of different battery technologies.

First and foremost lithium is mainly found in small amounts in the Earth's crust, leading to high prices, long transports and other undesirable complications connected to mining industry, such as humanitarian concerns regarding the workers as well as the environmental impact. Sodium on the other hand is one of the most abundant elements in the earth's crust and in the sea, making it both cheaper and more environmentally friendly to extract [3]. Worth mentioning is that some lithium is present in soil and seawater as well, and there exist methods to extract it, but the low concentrations prove a challenge [8]. The concentration of sodium as compared to lithium in the earth's crust is 23600 ppm to 20 ppm, this combined with an overall higher cost for extraction and purification of lithium as compared to sodium, makes this option rather undesirable [9].

Another benefit of SIBs is that unlike lithium, sodium does not alloy with aluminium at low potentials, allowing for both current collectors to be made from inexpensive aluminium. LIBs require the current collector at the anode side to be made from copper, which is significantly more expensive and also dissolves into the electrolyte below a certain voltage, thereby destroying the battery. SIBs do not show this behaviour since aluminium does not dissolve into the electrolyte even after full discharge to 0 V, allowing for safer storage and transportation [10].

Since the LIBs have been firmly integrated into the industrial apparatus over the years, SIBs have a great opportunity as a "drop-in" technology, since all the principal components are very similar, and a battery factory could with minimal adjustment transition to production of either battery [4]. At least this is considered a possibility, although there are many aspects to be considered and investigated before one can say whether it is feasible and/or lucrative.

One of the problems with SIBs is the not yet fully understood internal mechanisms, this in turn slows the development and improvement of the technology [11]. Comparing a well developed commercially available LIB, with 350 mAh/g of specific capacity, to a hard-carbon SIB with 250 mAh/g, which corresponds to $Na_{0.67}C_6$ formation at 0.25 V versus Na/Na^+, we see that there is still some improvement to be made [9]. Comparing energy density instead, a commercially available 18650 LIB will range from 530 to 785 Wh/l, whilst an 18650-size cell SIB reported by the French research agencies CNRS and CEA has 250 Wh/l [9]. The aforementioned SIB might be considered the most advanced commercial cell of its kind, but no information on electrode or electrolyte materials is provided [12].

To truly be able to improve this capacity and enhance other aspects of the SIB technology we need to deeply understand the mechanisms at play, and there has been a lot of research for elucidating these mechanisms [13–22]. Of particular interest is the formation of the solid electrolyte interphase (SEI), which is formed in the first few cycles of the battery due to degradation of the electrolyte.

Another mechanism of great importance is the intercalation of sodium into the anode structure. In LIBs the preferred anode material is graphite, and it is highly structured and allows for good and predictable Li-ion intercalation. Graphite does not produce any reasonable capacity for SIBs, and the to date most promising anode material for SIBs has been hard-carbon (HC), sometimes referred to as nongraphitizable carbon [23]. HC has an amorphous structure with some highly ordered domains, making it rather unpredictable. The production of HC is very simple and it can be derived via pyrolysis of coconut husk or banana-peels [24, 25], as well as other organic materials, making it very cheap. Due to its highly disordered structure it is susceptible to change with varying production methods, temperatures and precursors. While not posing a great difficulty when considering large scale production, it is a hindrance when it comes to research. Many articles only mention that HC is used as an anode, while many factors such as porosity, loading etc. can have great impact on capacity and cycling characteristics, thus making comparisons in literature harder.

The sodium storage mechanism into HC is thought to be constituted by three main processes: edge/defect site occupancy, intercalation and pore filling [13–22]. The different mechanisms are illustrated in figure 1.1. The debate is mainly as to what occurs when, the voltage profile for sodiation/desodiation is well known, the challenge is in correlating and interpreting data to fit this curve. The voltage profile will usually have a linear decrease in potential until reaching approximately 50% of capacity (this is usually referred to as the sloping region), which usually constitutes the majority of the voltage drop (down to 0.1 V), and it is then followed by a plateau that stretches over the remainder of the capacity as seen in figure 1.2 (called the plateau region).

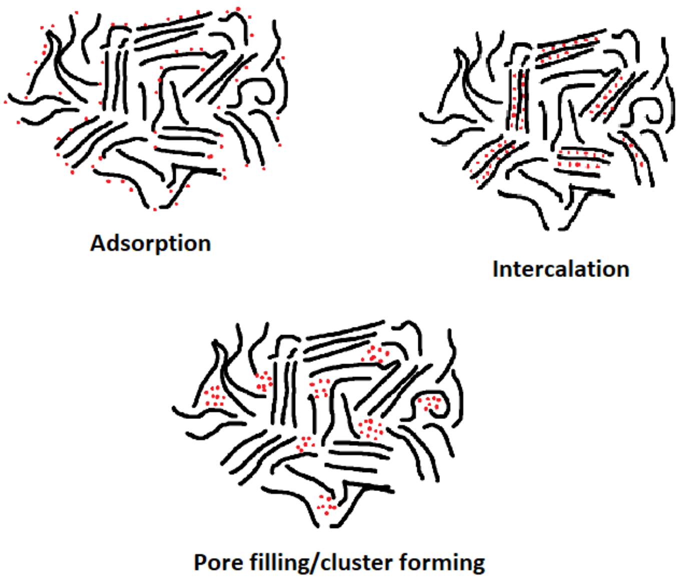

Figure 1.1: The three main processes for Na^+ (shown as red dots) storage into HC.

These two different regions have been investigated using diffusion coefficient measurements, different NMR techniques, small angle X-ray scattering just to mention a few, but no consensus on the mechanism has been reached [15].

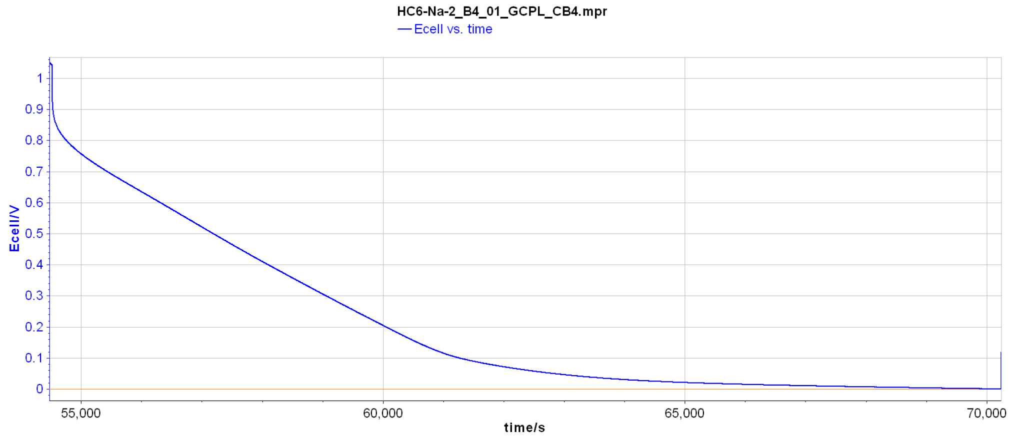

Figure 1.2: The voltage profile for the discharge of a SIB. Cycle 1 at charging/discharging rate C/10. These curves will have a different appearance depending on anode material used, this one is for the HC used in this study. More information in section 3.1 (Electrochemical cycling and cell build).

1.1 Battery monitoring

To be able to monitor these battery systems different optical sensors have been investigated [26]. The optical sensors allow for *operando* measurements by placing the sensing part into the actual battery. This allows not only for measurements at the highest value location, but also real time monitoring. Considering these benefits from optical sensors, the step towards using them for *operando* mechanistic studies seems small. Optical sensors are not the only option being explored, electrochemical impedence spectroscopy (EIS) [27–29], and remote query measurement [30–32] are a few techniques falling under the category contact measurement, just like the optical sensors. Contact measurements are characterized by the direct sensing, which in turn reduces the need for complex and computationally demanding algorithms used in contemporary systems [33]. More importantly than potentially reducing the computational load, is reducing the need for algorithm based estimations, and relying on actual measurements instead.

1.2 Aim

The aim of this project is to incorporate fiber optic sensors into SIBs to better understand the storage mechanism of sodium-ions into HC in SIBs. This will be done by implementing fiber optic sensing, using the nanoplasmonic sensing (NPS) technology developed by Insplorion AB (Gothenburg, Sweden). The fiber optic sensor will be embedded into the battery, allowing for measurements of internal chemical events. *Operando* measurements will then be conducted to be able to monitor battery internal processes in real time. The batteries will undergo electrochemical cycling while measurements are carried out, hence *operando* measurements. These two datasets will then be compared to find correlations between signal and mechanism. All the steps leading up to mechanism determination will be documented and evaluated. Thus a sizeable amount of this study focuses on findings and method development along the way.

A rigorous approach will be taken where each component of the system is investigated before moving on to *operando* measurements. Based on these findings and literature research, an attempt will be made to shed light on the mechanism at play, and the possibility to measure it. A considerable amount of research has been done on the subject, but no real consensus has been reached, hopefully this study will be another brick in the building of a complete understanding of the mechanism.

1.3 Limitations

This study is limited to using voltammetric data provided by the cycling unit as well as the optical data aquired by the spectrometer. Whilst it would have been beneficial to perform further studies on the HC anode, there is published data available which is used in this report [34]. The optical data could have been attempted to be verified via a greater range of different system combinations, such as different sensors or battery assemblies. Autopsies of cycled batteries could have been attempted for further information as well. The comparisons made to existing mechanistic theories found in this report are purely based on comparison to literature. Deciphering the raw optical data is very difficult due to the complexity of the system measured.

Another limitation to drawing final conclusions is the use of half cells in this study. By using pure sodium metal as the cathode material, the contribution from any structure or chemical components to the system can be ruled out. Especially since a part of the focus is to investigate the anode properties, this is beneficial. For applying the findings to an actual working full cell on the other hand, this approach will limit the usability of the data.

2

Background and Theory

The following sections give a short introduction to the batteries being studied and the sensors used for this. Furthermore some of the mechanisms proposed for HC sodiation in the literature will be introduced.

2.1 Batteries

While batteries have been around for a very long time, we make certain distinction between something like a voltaic pile, which was invented by Alessandro Volta 1800, and a rechargeable battery. Since electric current in batteries is based on the electric potential between two electrodes and their ion and electron transport pathways (like a simple lemon battery), the battery will be consumed once the starting materials have reached equilibrium [35]. This type of battery is referred to as a primary battery. Secondary battery technologies were later developed where the application of a reversed current charges the battery by reversing the ion flow. The first secondary battery was a lead-acid battery invented by Gaston Planté in 1859 [36].

The use of these secondary batteries has been widespread and soon more energy dense solutions were researched, leading to the development of the lithium ion battery (LIB) by Sony Co. in the 1990s [37]. The following 30 years this technology has been commercialized, optimized and integrated into other technologies. But with increased global usage some limitations of the LIBs become apparent. Among other the mining of lithium is limiting. Adding to this limitation, the climate change pushes the development for green alternatives to fossil fuels, such as wind and solar. These energy technologies are of a stochastic nature, leading to the necessity of grid stabilization and energy storage [38]. Together with the development of more electric vehicles the demand for batteries is higher than ever. This is reflected in the research done in the field, there were 119188 new publications on batteries from 2010 to 2017 [37]. This corresponds to a 260% increase in total literature volume on the subject in that time span according to a search on the Web of Science online database. Compared to other published literature in the same period, battery research experienced 4.5 times the percentual rate of growth.

The battery research is divided between those further striving to enhance the lithium based technologies and those looking for new alternatives. The alternatives to LIBs are among others, battery systems based on sodium, magnesium, zinc and aluminium, of which the sodium systems show the greatest promise to be able to replace the current LIBs [39]. The aforementioned battery systems are based on the same working principle as LIBs, although different approaches exist, for example flow batteries [40] and metal-air batteries [41], just to mention a few.

2.1.1 Sodium-ion batteries

There is a lot of research going into greener alternatives to LIBs [4], and the obvious choices to replace Li are some of the elements surrounding Li in the periodic table, such as Na and K for example. These elements share some important traits such as low ionization energy, and can be used in batteries in a similar manner to Li. The SIBs have shown great promise for a number of reasons, mainly abundance and cost efficiency of raw materials. LIBs require an expensive copper current collector at the anode side due to an alloying process between lithium and aluminium at low potentials, something that cannot be observed for sodium aluminium systems [42]. Therefore a more inexpensive aluminium current collector can be used on the anode side as well as on the cathode side in SIBs. The stability of the system allows for storage and transport at 0 V. This has a great impact on improved shelf life, but the main benefit is the ease of transportation, which furthermore is beneficial for global commercialization.

Comparing SIBs to LIBs, there are some intrinsic differences, among others the ionic radius, 1.03 Å for Na^+ and 0.71 Å for Li^+ [23]. The electrochemical potential is also different, 2.71 V vs. standard hydrogen electrode (SHE) for Na/Na^+ and 3.04 V vs. SHE for Li/Li^+. These differences play a large role when considering suitable electrolytes, anode materials, and final applications based on performance. See section 2.1.2 (Hard carbon), for more information on how the anode material needs to be adapted to suit Na^+ storage. The working voltage of the battery is of course affected by the difference in electrochemical potential, reducing the output voltage of a single SIB cell. Nevertheless, a lower voltage also opens up a greater range of possibilities for electrolytes, since the stability under applied voltage is not as constrained as in the LIB-systems.

Considering capacities, a SIB based on HC has the theoretical capacity of 279 mAh/g, based on the assumption that the intercalation compound formed is NaC_8 [43]. This is the most used reference capacity in literature, although higher capacities can be achieved. Wen et al. showed that expanded graphite with an interlayer spacing of 0.43 nm could deliver 284 mAh/g at a current density of 20 mA/g [44]. This suggests that the intercalation contribution to the Na^+ storage reaches it limit at 279 mAh/g, as calculated, but that there are more factors at play. More on this in section 2.5 (Sodiation mechanism). There are much higher capacity alternatives as well, such as the red phosphorous anode, which is theoretically capable of 2596 mAh/g [45]. However, due to a number of limitations including large volume expansion and poor conductivity, the system is not ready for use.

2.1.2 Hard carbon

Many different options have been considered and investigated as anodes in SIBs [11]. A wide range of materials has been tested, including carbons [46–49], oxides/sulfides [50–52], phosphorous[45, 53, 54] and alloys [55, 56]. Among these the HC anodes have distinguished themselves as the most promising alternative due to their low cost, ease of production and non toxicity in tandem with a reasonably high capacity [22].

The behaviour of different types of graphitizing carbons and their temperature dependence during synthesis has been investigated in the first half of the 1900s [57]. It was as early as 1934 that graphite-like structures were found in carbon black materials [58]. The most common anode material for LIBs is graphite, which has an interlayer spacing of 0.33 nm, and even though the Na ions are theoretically small enough to fit in between the layers, experiments with electrochemical/vapor intercalation have shown that it only produces a capacity of 31 mAh/g [59]. Instead the material mainly used for SIB anodes is HC, which is amorphous and varies greatly based on synthesis procedure [60]. Depending on the pyrolysis temperature the HC will exhibit varying degrees of graphitization, Sun et al. propose a differentiation between purely disordered, pseudo-graphitic and graphite-like regions in the material [22]. They define disordered carbon as having above 0.40 nm d-spacing, pseudo-graphitic as having a d-spacing between 0.36 and 0.40 nm and the graphite like will as mentioned above have a d-spacing of 0.33 nm. There are also other structural details arising from different concentration of defects and impurities in the material, depending mainly on the precursor used in the synthesis process [22, 24, 60–62].

2.1.3 Solid electrolyte interphase (SEI)

In a battery based on alkali and alkaline earth metals, these are always covered by a thin surface layer, created by the reaction between the electrolyte and the metal [63]. This surface layer has the properties of a solid electrolyte, still capable of ion transport, although it provides stability to the electrode. Because of it acting as an interphase between electrode and electrolyte, it is referred to as the solid electrolyte interphase (SEI). The SEI is also present at the anode side, where it plays a vital role in hindering anode decomposition into the electrolyte [64]. The SEI is formed during the first cycles in a battery and it affects a multitude of factors, such as metal electrode corrosion and reaction kinetics [65].

2.1.4 Sodiation mechanism

As mentioned in the introduction there are a number of theories regarding the Na ion storage mechanism into HC, but no consensus on which of them is correct.

The first proposed mechanism was put forward by Stevens and Dahn [66–68], and suggested an insertion-filling mechanism. The first step of the mechanism would be the insertion of Na^+ into the parallel graphitic layers. This step would correspond to the sloping region of the voltage profile as seen in figure 1.2. The following plateau region was then attributed to the filling of the nanopores of HC. This conclusion was drawn from *in-situ* small angle X-ray scattering (SAXS) measurements indicating that the scattering from the nanopores decreased once reaching the plateau region, suggesting the nanopores filling up with Na^+. This theory was backed up by Komaba et al. [18], analyzing commercial HCs using *ex-situ* X-ray diffraction (XRD), SAXS and Raman spectroscopy. Again, after discharging to 0.1 V, the Bragg peak from X-ray measurements shifted to a lower angle from 23.4° to ca. 21-22°, suggesting Na^+ insertion into graphitic layers during the sloping region. The Raman spectroscopy showed a red-shift during the sloping region, but no shift in the plateau region, further strengthening the proposed theory. A red-shift means a change that corresponds to a change from higher to lower wavelengths.

Another study by Zhang et al. employing X-ray spectroscopy found no shift of the Bragg peak during the discharge process while performing *in-situ* measurements of polyacetonitrile-derived HC [69]. Instead a new mechanism was proposed, the adsorption-filling mechanism correlates the sloping region to two different mechanisms depending on the HC structure, and the plateau region to mesopore filling. Samples prepared at temperatures exceeding 1000 °C show greater amounts of mesopores, as well as a more significant contribution to the capacity of the plateau region. The plateau region therefore still exhibits a pore filling mechanism as previously thought. The sloping region is thought to be a combination of two adsorption mechanisms, one being Na^+ adsorption at heteroatom defect sites, mainly N and O. A decrease of these heteroatoms gave rise to a loss in capacity during the sloping region. The other mechanism during the sloping region is Na^+ adsorption on the disordered graphite sheets, but due to the broad Bragg peak, Na^+ intercalation cannot be entirely ruled out. There are more studies supporting the adsorption-filling mechanism with minor adjustments to the theory [70, 71]. There are some deficiencies in the filling-part of the theory since the storage mechanism in this part is thought to be dependent on porosity, there are some contradicting studies. For example, some HCs have been found to have a smaller amount of pores when increasing the pyrolysis temperature, while at the same time experience an increase in plateau capacity [25, 71].

The third, more renowned mechanism is the adsorption-insertion model proposed by Cao et al. [72]. By investigating Na^+ storage into hollow carbon nanowires produced by pyrolyzing polyaniline, the storage mechanism of Na^+ below 0.1 V can be observed to be similar to that of Li storage into graphite. Calculating the energy cost based on the carbons interlayer spacing of 0.37 nm and the energy barrier of 0.053 eV, the insertion of Na^+ is likely. Ding et al. was the first to observe a reversible d-spacing expansion and contraction in the HC derived from peat moss, using *ex-situ* XRD [73]. Since this layer dilation is analogous to the behaviour of graphite upon Li intercalation, the mechanism has by many been believed to rule out the pore filing alternative [25, 73, 74]. Sun et al. proposed an "Extended adsorption-insertion" model, which fills some gaps from previous work and offers an approach to theoretical capacities of HC [22].

A more recent study by Stratford et al. tries to find a framework into which HCs can be categorised, allowing for more accurate comparisons between different studies [75], introducing a new concept of "average local structure", and defining this as a region consisting of two parallel graphene fragments. To model these average structures, pair distribution function analysis (PDF) and derivative PDF (dPDF) are used. For the sloping region this study proposes two different mechanisms, beginning by addition of Na^+ near the surface of the HC. This results in carbon layer expansion due to electron donation from the Na, making the interlayer spacing and split pores virtually indistinguishable. During the plateau, cluster forming is believed to be the dominant contribution to the capacity, which is confirmed by solid state NMR, displaying a "Knight-shift" which is indicative of metallic sodium forming. The proposed mechanism is therefore intercalation-filling, which brings us almost all the way back to the mechanism suggested by Stevens and Dahn [66–68, 75].

2.2 Electrochemical cycling

Galvanostatic Cycling with Potential Limitation (GCPL) is a method where the battery is charged and then discharged with a constant current over several cycles. The speed of these cycles is determined by the C-rate, which is defined as the applied (constant) current that will fully charge an empty battery during one hour. Of course this also applies to discharge, so a full charge/discharge cycle at 1-C takes two hours. Slower C-rates operate at lower currents, so C/10 will take ten hours for a complete charge/discharge. The limits defining when a charge or discharge is complete are based on the potential, in the case of the batteries in this study, the limiting lower and upper potentials are 0 and 2 V respectively. The lower limitation is naturally the equilibrium state, but the upper limit is derived from the battery components stability in the electrolyte. Voltages well above 2 V may result in the decomposition of the components, and to stay perfectly safe the 2 V limit was chosen [76].

For determining the cycling current, the capacity of the battery needs to be known, then the applied current to achieve a certain C-rate can be calculated according to equation 2.1, where mA is the current in milliamperes and h is the time in hours.

$$\frac{Capacity(mAh)}{Cycling\ time(h)} = Applied\ current(mA) \tag{2.1}$$

2.3 Fiber optic sensors

With the increasing demand for electricity, specifically green energy, used for grid applications as well as transportation, batteries have a big role to play. Optimization of these batteries, both in production and in application, relies on accurate measurements of the batteries internal components. In application this is represented by measuring systems determining the state of the battery and feeding this to a battery management system (BMS), which will optimize the use of the battery while having safety switches for extreme conditions. To gain all this information, contemporary BMS systems use measurements like voltage, current and temperature information to compute parameters like state of charge (SOC) and state of health (SOH) [77]. These measurements are based on electrical connections, which may suffer from electromagnetic interference. Furthermore, these measurements cannot be taken within the cell structure, leading to delays and poor convergence with BMS algorithms [26]. As mentioned in the introduction there are methods for improved battery measurements not relying on fiber optics, such as EIS [27–29] and remote query measurement [30–32], but they lie outside the scope of this work.

To solve aforementioned problems with the traditional measuring systems using electrical connections, a number of different fiber optic sensors have been investigated, for example fiber bragg grating (FBG) sensors and fiber optic evanescent wave sensors [26]. Fiber optic sensors possess some inherent features which make them desirable for battery monitoring, such as being electrically insulated and immune to electromagnetic and radio frequency interference, as well as being small enough to be inserted into a battery almost without changing overall size and weight of even smaller cells [78]. Over the last five years the fiber optic sensing for battery applications has made up 32% of the published articles regarding new battery monitoring technologies. This showcases the recognized potential of the technology.

In this study an optical fiber with a metallic nanostructure enabling plasmonic resonance will be used for measurements. More on the sensing structure in section 2.4 (Nanoplasmonic sensing(NPS)). This nanoplasmonic sensor possesses many of the aforementioned desirable traits of fiber optic sensors. While the different sensors mentioned earlier in this section focus on on-board sensing, and the NPS sensors also are mainly focused on fulfilling that specific function, this study will use the technology for research and development work which in this case is inherently different from the on-board application. Therefore the outcome of the sensors suitability for this task will be evaluated.

2.3.1 Nanoplasmonic sensing (NPS)

Most of us are familiar with the particle-wave duality where a photon can be described as either a wave or a particle depending on our observation [79]. The same kind of phenomenon can be observed in the electron field composed of delocalized electrons found in metals. The oscillations in the mechanical vibration of the electron field can be described and quantified into a quanta, called a plasmon. There is a phenomenon called surface plasmon resonance (SPR), which is the foundation nanoplasmonic sensing (NPS) is based upon. Nanomaterials exhibit uniquely different properties from their bulk counterparts since the scale reaches the limit for some physical phenomena. Therefore many fundamental processes become size/thickness and shape dependent [80].

NPS enables measurements at the nanoscale without the need for invasive high-energy methods such as electrons, neutrons or X-rays, having high enough energy to affect the true equilibrium, or leave artifacts in the material measured. Instead the SPRs can be read by the means of low-energy optical spectroscopy, resulting in minimal impact of the measurement [81].

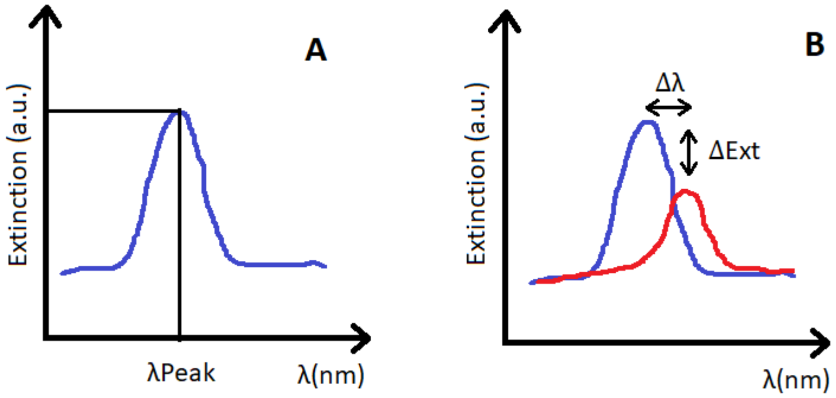

Figure 2.1: Schematic illustration of the working principle of NPS. A: The plasmonic peak and its correlation to wavelength. B: The effects of changing the refractive index of the material surrounding the plasmon, from low RI (blue line) to high RI (red line).

The surface plasmons (SPs), can interact with photons of a wavelength matching the SPs resonance condition. When the plasmon is excited it will absorb and scatter the incoming light, which can be seen as a peak in an extinction spectrum as illustrated in figure 2.1. Figure A is highlighting how a specific wavelength produces a peak extinction at the wavelength λpeak, figure B shows the two most useful readouts of the optical signal upon changing the plasmons resonance conditions, that is change in λpeak ($\Delta\lambda$) and change in Δextinction (ΔExt).

For most plasmonic sensors Au is used for its nobility, ensuring chemical resistance in many measuring environments. Furthermore Au displays a narrow and well defined plasmonic peak, allowing for clean and easy to read spectrum. The plasmons are sensitive to their dielectric surrounding thanks to the strongly enhanced electromagnetic fields in the direct proximity of the nanostructures. Through such enhancement, plasmon resonance sensitivity depends on the tiny variations in their surrounding dielectric medium. The plasmons can interact with the photons traveling within an optical fiber, thus producing an easy and fast way to monitor everything the plasmons sense. The greatest weakness of this system is that there is only one readout, but not necessarily only one process that is being measured [81]. In effect this means that the signal lacks specificity, it can tell that it senses something but not what it is. Therefore a framework of other methods needs to exist to be able to verify what happens in the system subject to analysis, alternatively the system needs to be so well known that there is no doubt as to what is actually being measured.

2.3.2 NPS applied to battery sensors

The NPS technology is compatible with optical fibers, by physical vapor deposition (PVD) the gold structure can be applied to the optical fiber. The instrument used for the fibers in this study is a FHR MS 150 Sputter. Sputtering is a class of thin film technology based on the material to be deposited being bombarded with plasma ions, vaporizing it. The gaseous material can then be uniformly condensed onto the substrate surface [82]. The coating can be done selectively while the fiber rests on a surface, allowing for a one sided coating or a two sided one if desired. This allows for further selectivity, since the sensing structure can be turned towards a specific location of interest within the battery. Noteworthy is that without any sensing gold structure at all, the fibers are still able to sense their surrounding quite efficiently, much like an evanescent wave sensor would [26].

To ensure the sensor remains unaffected by chemical events or current inside the battery, a fluoropolymer coating is applied to most sensors in this study before testing. A number of cells in this study are cycled with uncoated fibers as well to investigate the effects of the coating. Current might affect the sensor via plasmoelectric effects, which is a relationship between plasmons and charge. Warren et al. has shown that plasmons produce a current under light irradiation and vice versa [83]. In the case of the cells investigated in this study, the plasmoelectric contribution to the charge in the battery might be considered negligible, although the plasmons are more likely to be affected by the charge in the battery.

3

Materials and methods

The system that is studied in this report is very complex due to the possible interactions between the fiber sensor and the battery components. To be able to understand all the components, how they perform, and how they will contribute to the collected signals during *operando* measurements, they will initially be studied separately. First the sensing fibers are tested, then the batteries, and finally they are assembled and tested together. The cells in this study are half cells, which enables the exclusion of any disturbances from cathode contribution to the system.

3.1 Materials

The HC used in this study was kindly provided by Beda et al. [60] table 3.1. The HC was dried in a kiln for 2-3 hours at 100° C, before assembly of any cells. The parameters available for the electrode material from Beda et al. [60] is seen in table 3.1. It is a commercially available hard carbon called PAC2 from Aekyung petrochemical, South Korea. This commercially available electrode material has according to Beda et al. a reversible capacity of 278 mAh during the first cycle, and a 14% initial irreversible capacity.

Table 3.1: The parameters for the HC used [60]. Listed to the left is a short explanation to the measurements, for further information please refer to the original article.

Property	**Value**
Part. size (μm)	5-10
Interlayer spacing d002 (Å)	3.75
Specific surface area N_2 2 SSA (m^2/g)	3.8
Specific surface area CO_2 SSA (m^2/g)	3.6
Active surface area ASA (m^2/g)	6.4
Oxygen based surface groups COx (mmol/g)	0.070
Tap density (g/cm^3)	0.96
He Tap density (g/cm^3)	1.95
Electrode porosity (%)	46

The sodium used was bought from Sigma Aldrich as cubes in mineral oil, 99.9% trace metals basis. For cleaning the cubes from oil hexane was used, also purchased from Sigma Aldrich, laboratory reagent grade >95%. The separator material used was a Whatman glass fiber filter which was dried in the same fashion as the HC (2-3 hours in a kiln at 100° C). The electrolyte is 1 M hexafluorophosphate ($NaPF_6$) in EC:DMC(1:1) by weight. The battery casings and other metal components of the cell were made from stainless steel.

For the fibers a multimode optical fiber was used. For more on the sensor fabrication see section 2.4.1 (Applied to battery sensors).

3.2 Methods

Below the different methods and procedures for measuring and data processing are introduced.

3.2.1 Cell set-up and electrochemical cycling

Before the cells for *operando* testing were assembled the same principle as for the fibers was followed, the system was simplified for easier optimization and troubleshooting. The first step was to ensure proper cell handling and operating procedures using LIBs, the reasoning behind this is to train on a similar system without wasting for example hard carbon. After three successfully cycling lithium iron phosphate (LFP) cells, the focus was moved onto SIBs. The SIBs constructed will serve as reference cells to be able to compare how the fiber might affect cell stability and performance.

The cells for *operando* measurements are built in two stages, first outside of the glovebox, and then under argon atmosphere inside the glovebox where oxygen and water content was kept <10ppm. The first step consists of drilling a hole through the casing to allow for the optical fiber to pass through. This was done with a 0.8mm carbide drill in a Proxxon drill press, drilling from the inside out while the casing is supported by an angled holder. This allowed for the burr created by the drill bit to be pushed to the outside where it would not interfere with internal components such as the gasket, and more importantly the fiber. This method proved superior to drilling from the outside in, which required further polishing and cleaning up of the hole. After drilling the casing, the fiber sensor was installed and secured with tape to ensure proper alignment with the drilled holes. The alignment is crucial to success since a misalignment during crimping of the cell certainly will lead to breaking the fiber, and it is very hard to do inside the glovebox due to thick gloves and lower visibility. After inserting the lower casings with their attached fibers into the glovebox the rest of the components are added according to figure 3.1. First the gasket is put in place, followed by the HC anode with a diameter of 14 mm which needs to be slipped under the fiber. Then the separator measuring 17 mm in diameter is added and soaked with 60 μl of the electrolyte. Thereafter a 15 mm in diameter Na metal cathode is brushed with a toothbrush to ensure cleanliness and lack of oxides upon assembly, then spacer, spring and upper casing are added to enclose the cell. The assembled cell is then put into a hydraulic crimper and put under 70 kg/cm^2 of force to permanently close the battery. As a last step a small amount of 5-minute epoxy was prepared and used to seal the drilled holes were the fiber protrudes to make sure no contaminants reach inside the battery. The battery was left for the glue to cure in the glovebox.

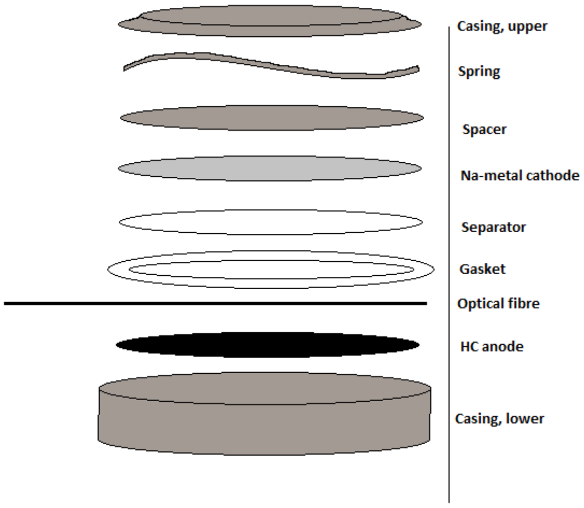

Figure 3.1: Components of battery cells for *operando* measurements.

The cells were then connected to the electrochemical cycling equipment, a Biologic (BCS-805 and BCS-810), as well as an Insplorion M8: 8-Channel Analyzer. The connection of the fibers is explained in section 3.3 (Bulk refractive index sensitivity (BRIS)). The program used for cycling is shown in table 3.2, and is designed to give a wide variety of C-rates to analyze, as well as a number fast cycles (C/1) to age the battery to some extent and evaluate the fiber performance under these conditions. This cycling program was not the first one used, and some cells seen in the results have been cycled using a similar program with the single difference being that the two C/10 cycles at the beginning are not part of the looping. Meaning that step number 17 in table 3.2 would read "Steps 5-16 x 4" instead. The Insplorion 8-Channel Analyzer software is amongst others used to adjust the integration time, ensuring a photon count of approximately 30000, regardless of possible defects in the spliced fibers.

Table 3.2: Cycling program, where CC is constant current.

Step number	Type	Mode	C-rate	Voltage cut-off
1	Discharge	CC	C/10	0V
2	Charge	CC	C/10	2V
3	Rest	5 minutes		
4	Repeat	Steps 1-3 x 2		
5	Discharge	CC	C/5	0V
6	Charge	CC	C/5	2V
7	Rest	5 minutes		
8	Repeat	Steps 5-8 x 4		
9	Discharge	CC	C/2	0V
10	Charge	CC	C/2	2V
11	Rest	5 minutes		
12	Repeat	Steps 9-12 x 4		
13	Discharge	CC	C/1	0V
14	Charge	CC	C/1	2V
15	Rest	5 minutes		
16	Repeat	Steps 16-18 x 4		
17	Repeat	Steps 1-16 x 4		

3.2.1.1 Capacity fade determination

An important characteristic of batteries is their deterioration over time, this can be due to electrolyte degradation amongst others [84]. It is of course desirable that this deterioration, collectively labeled capacity fade, is as slow and as small as possible, therefore it becomes a good measure for how well your batteries are performing capacity-wise. *Operando* measurements mean little to nothing when performed on a system that is not functional, therefore the capacity fade is investigated for the different batteries used.

As we can see in 3.2, there are several platforms following a pattern, these correspond to the different C-rates. The cycling starts off at C/10 which is the curve we see coming from the top, then the program follows a rythm of four C/5 cycles, four C/2 cycles and four C/1 cycles to then restart at C/5. Each plateau is hence comprised of four datapoints. The harder the battery is pushed, meaning higher charge amperage and higher C-rates, the lower the capacity will be due to the ions' inability to move fast enough, and the lack of time for the entire system to stabilise. No permanent damage is done to the system, it simply does not operate as well under these conditions, which is why the capacity rises once more as soon as the C-rate drops. The previous sentence is apparently not entirely true, because the following C/5 plateau is not as high as the last one. This is the capacity fade, but it makes no great sense to compare it across C-rates, instead the value from each plateau is taken early on, and the same corresponding plateau is then measured a few cycles later.

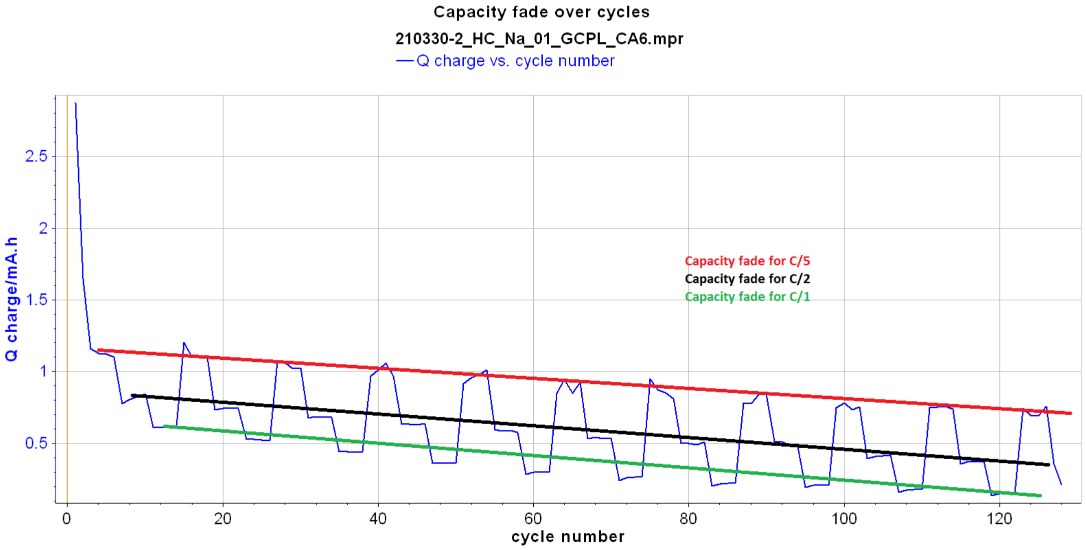

Figure 3.2: The capacity fade for different C-rates as a function of cycling. Lines to guide the eye only.

3.2.1.2 Dip coating of fibers

Some fibers were coated with a fluoropolymer to protect the sensing structure from the harsh environment inside the battery as well as from the plasmoelectric effect. The fibers were first cleaned for 10 minutes in an ozone cleaning device, then dip-coated with a submersion and extraction speed of 40 mm/min, and a hold time of 3 s. Great care was taken as to not allow the wet fiber touch anything (in the region of the sensing structure) during the curing process. The curing consists of 15 minutes at 80°C followed by 30 minutes at 180°C.

3.2.2 Experimental set-up, optical measurements

Two different setups have been used, one for BRIS measurements and one for *operando* measurements. The optical part of the measurement remains the same, apart from only one channel being needed during BRIS experiments, therefore omitting the 8-channel optical switch. Otherwise the setups are much the same, one having connected leads for the voltammetric equipment and the BRIS measurements not having them, therefore the splicing procedure will be explained only once for BRIS-measurements.

3.2.2.1 Bulk refractive index sensing (BRIS)

A method commonly used to assess sensor performance in solution is called BRIS, it consists of measuring the ratio between sensor output changes to the change in refractive index. When experimenting with different fibers this is an invaluable tool to get basic information regarding a sensor without having to go through the rather lengthy setup and preparation for *operando* measurements.

The connection between the fiber from the instrument and the fiber sensor is achieved via fusion splicing. The instrument used for this is a fusion splicer made by Furukawa electric, model: fitel ninja NJ001. The ends of the fibers are clamped within the instrument, then brought together and finally melted together by the means of an electric arc. Prior to this process the fiber ends need to be stripped of any coating and cut to produce a good edge for fusion splicing. Two different fiber coatings were used in this study, one composed of acrylate and the other of polyimide. The coating can be removed chemically or mechanically for the acrylate fiber, in this study the mechanical approach was taken due to the speed and simplicity of the process. The coating is stripped with a fiber stripper tool, much resembling a cable stripper, then it is cut with a fiber cleaver made by Ericsson model: EFC11-STD. The polyimide coating cannot be mechanically stripped and was therefore chemically stripped instead.

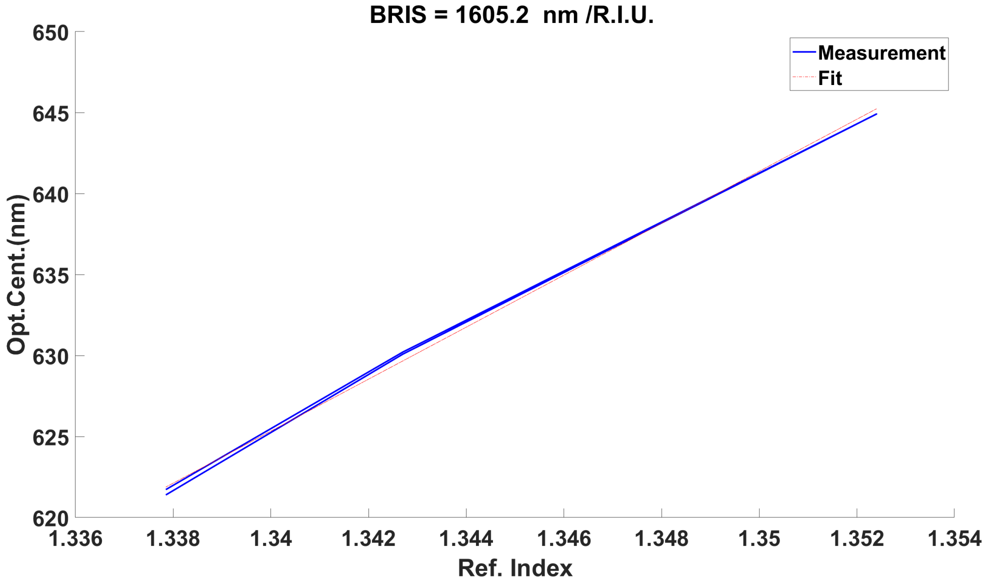

Figure 3.3: BRIS as measured from optical center in nm vs refractive index unit. The BRIS value is the slope of the model fitted to the curve.

The resulting BRIS value is given in $nm/R.I.U$ where R.I.U is Refractive Index Unit. This can be calculated by several different optical parameters such as peak position, extinction and optical center. In the case of BRIS calculation using extinction, the unit will be $Ext.(\%)/R.I.U$. The most reliable method was found to be optical centre, the reason for this is sometimes ill defined peaks in the spectrum. The optical center is the weight center of the spectrum. For this determination the optical signal is filtered using a Savitzky-Golay filter to smooth out the data, before any further calculations were made. The BRIS calculation is then performed as seen in figure 3.3, where the peak position as calculated by optical center is plotted against the known refractive index of the tested solutions. Then a linear function is matched to the plot, and the slope of this linear function is the BRIS. Due to complications when taking a reference spectrum in pure water, the measurement for 0% is taken during the time-span right before measurements, when the fiber is suspended in air. Figure 3.3 is derived from figure 4.1.

The sensing part of the fiber is approximately 1.5 cm long, and the fiber is bent into a small loop where the sensing structure is at the apex of the loop. This loop is then firmly affixed overhanging a table enabling a glass dish to be brought to the fiber. A schematic view of the set-up can be seen in figure 3.4, where the path of the light is indicated with arrows. With a pair of tweezers the surface tension is broken and the fiber is submerged into the liquid. For these tests a mixture of ethylene glycol (EG) and water is used in concentrations of 5%, 10% and 20 %. The test sequence is starting at 0%, represented by the fiber freely hanging in the air, and goes up to 20% and then ramps back down to 0%, which is to confirm that the fiber is not affected by residual solution. Based on the results it was decided that no rinsing between cycles is needed. The different concentrations of EG in water are used for changing the refractive index in the surrounding of the fiber. Water has a refractive index of 1.333 refractive index units (RIU) [85], and the different concentrations of the EG in water when measured with a refractometer, correspond to 5% = 1.339 RIU, 10% = 1.345 RIU and 20% = 1.350 RIU, which matches the numbers in figure 3.3 rather well. The refractive index values on the x axis of figure 3.3 are calculated from the fractions of water and EG and their corresponding refractive indexes as seen in equation 3.1, where A is the fraction of EG in %, 1.43 is the refractive index of EG and 1.333 is the refractive index of water.

$$RI = \frac{A * 1.43 + (100 - A) * 1.333}{100} \tag{3.1}$$

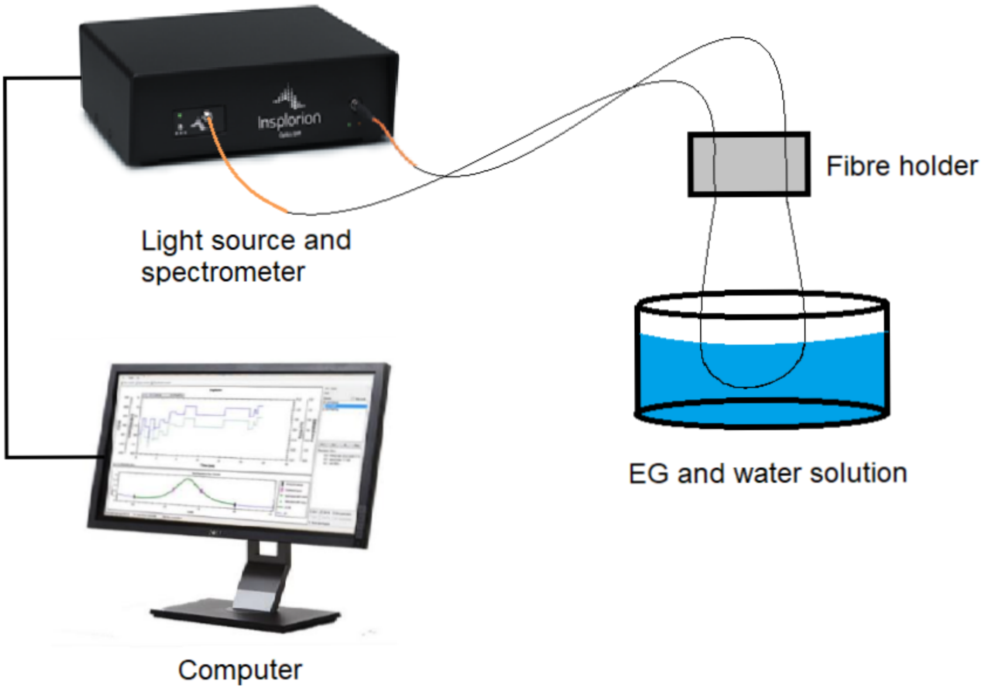

Figure 3.4: A simple schematic of the experimental set-up for BRIS-measurements.

The setup seen in figure 3.4 is not optimal due to the fact that the fiber is bent during measurement. This both affects the lights pathway and the surface density of the gold nano-film. In the case where the fiber only has the sensing structure on one side this effect is also highly dependent on fiber orientation. This bend is furthermore not present in the battery during *operando* measurements, and not as comparable as might be desirable. To negate these effects a new fiber holder was designed and produced using 3D-printing. The holder can be seen in figure 3.5, and is designed to be able to squeeze the fiber between two O-rings horizontally. This ensures the straightness of the fiber while allowing for liquid to surround the entire sensing structure. After clamping the fiber it does not need to be removed from the holder to change solutions due to the drain at the bottom, which can be opened to collect the previous solution, and then closed again to receive the next solution to be measured.

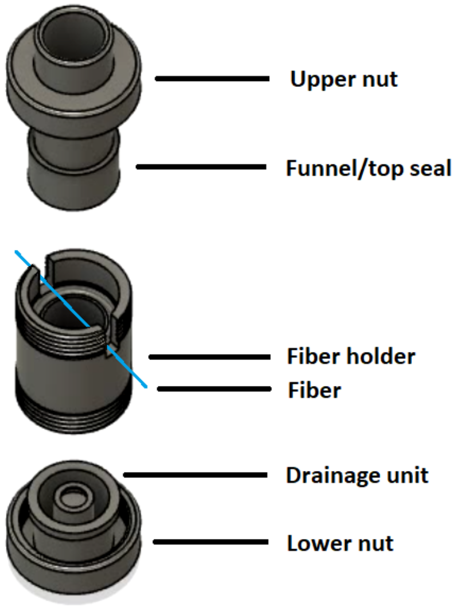

Figure 3.5: The final prototype of the new fiber holder. Fiber location highlighted by the blue line.

In spite of trying several different rinsing procedures, the signal remained affected. Furthermore, the signal was noisy as seen in figure 3.6 in spite of the holder sitting rigidly clamped in a holder. Due to the poor results this holder was abandoned.

3.2.2.2 *Operando* measurements

For the electrochemical cycling a Biologic (BCS-805 and BCS-810 with the BT-lab software V1.65) was used according to the tabulated program in table 3.2. As previously mentioned, the splicing for these measurements was carried out in the same manner as described in section 3.2.1 (Bulk refractive index sensing (BRIS)).

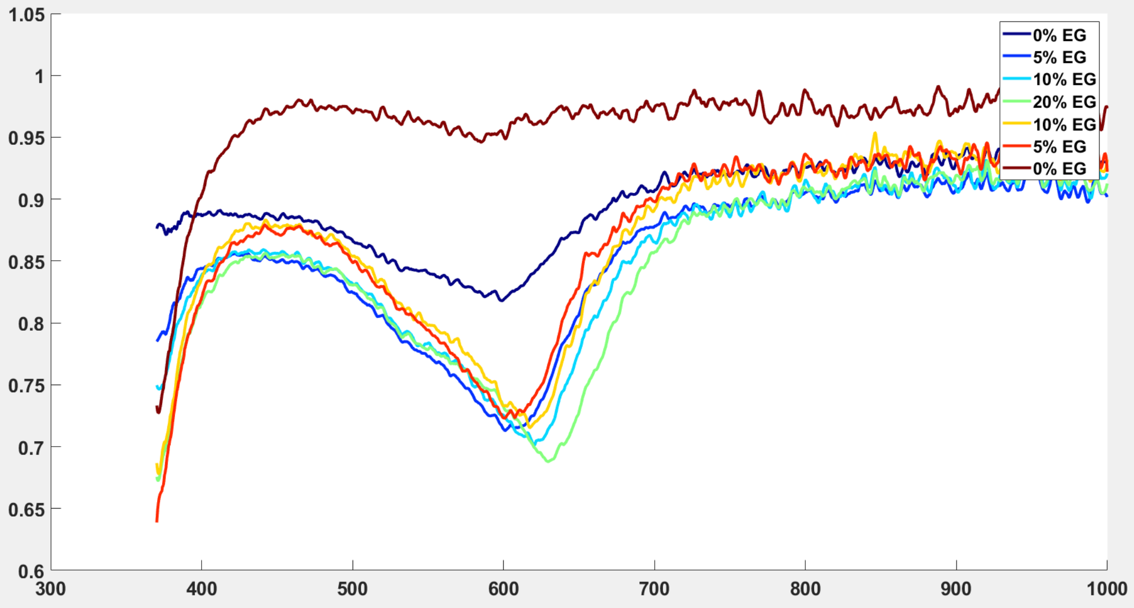

Figure 3.6: Transmission spectrum when using redesigned fiber holder.

For the spectral measurements an Insplorion M8: 8-Channel Analyzer was used, enabling simultaneous *operando* measurements for up to eight batteries at a time. Noteworthy is that the batteries were cycled in a room subject to sunlight through an adjacent window. Depending on the season, the temperature could change up to 3°C during the course of 24 hours. To reduce the influence on the fiber by sunlight and fluorescent lighting from light bulbs in the room, a box with a dark lining was placed over the cells whilst cycling. A perfect fusion splice should be affected as little as possible by the surrounding light, but in some cells a peak in the spectrum revealed the presence of stray light when the spliced region was uncovered.

3.2.3 Data processing

The data collected from the instruments is stored in .txt files which then are used in Matlab© for further calculations [86]. The majority of the code was provided by Athmane, the first supervisor of the project. Although some sizeable rewrites happened and new pieces of code were added during the course of the year, the large majority of the code was used as is. A complete check of the entire code is far beyond the scope of this thesis. The code will not be available in this thesis due to Insplorion AB (Gothenburg, Sweden), still using the code in their work to further develop their technology.

The electrochemical data is matched to the optical signal by time indexing, allowing for the detection of discrepancies or mismatches in the data set due to e.g. lag. The majority of the code is for sorting data parameters, and presenting them in different graphs, although a few calculations are made, which are explained below.

The optical center is calculated by integrating the area under the curve of the spec-

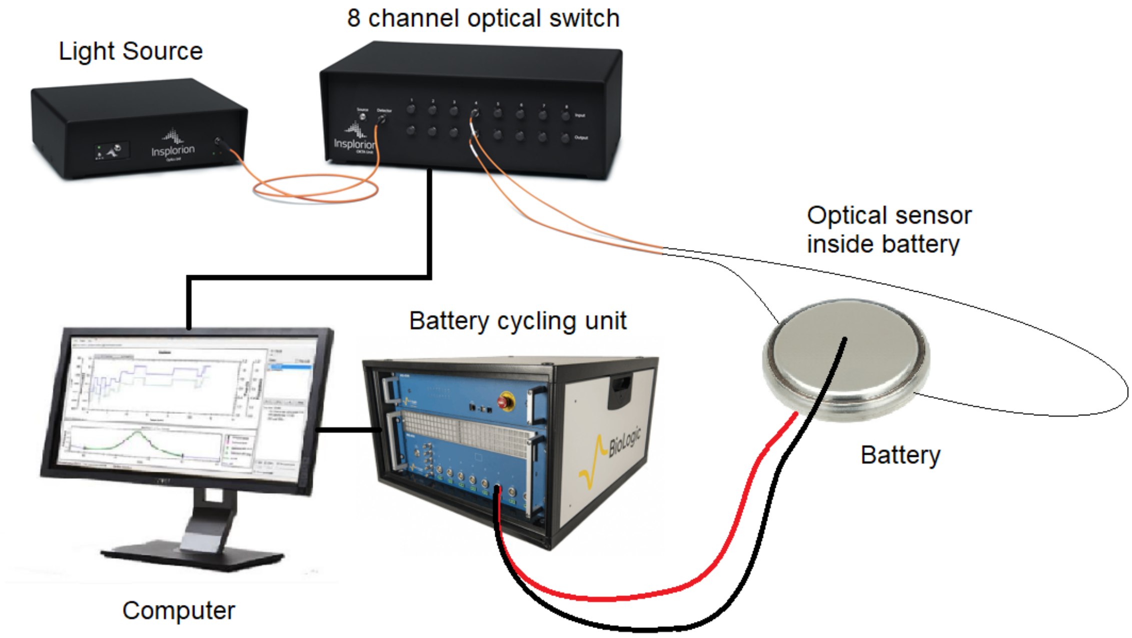

Figure 3.7: Schematic of the experimental setup for *operando* experiments. Red and black are the positive and negative leads respectively, and orange are the connectors to the optical fiber (in black).

trum and then finding whatever wavelength corresponds to half the area value [87].

State of charge (SOC) is defined in 3.2 and will usually be given in %. The available capacity is whatever capacity is available at that instance in time, while the rated capacity is the calculated max capacity of the cell.

$$SOC = \frac{Available\ capacity}{Rated\ capacity} \tag{3.2}$$

Depth of discharge (DOD) is defined in 3.3, and is essentially SOC reversed, where 100% DOD corresponds to a fully discharged cell, and therefore 0% SOC.

$$DOD = 1 - \frac{Available\ capacity}{Rated\ capacity} \tag{3.3}$$

4

Results and discussion

The results are divided into to the preparatory tests (BRIS and electrochemical cycling), before moving on to the *operando* tests. The first tests are performed to get an understanding of how the components function on their own to better be able to interpret the more convoluted and complex *operando* experiments.

4.1 BRIS

By reducing the system to a simpler state where the sensor preferably only senses one changing parameter, the performance of the sensor can be investigated. Extinction plots give information on response and signal stability.

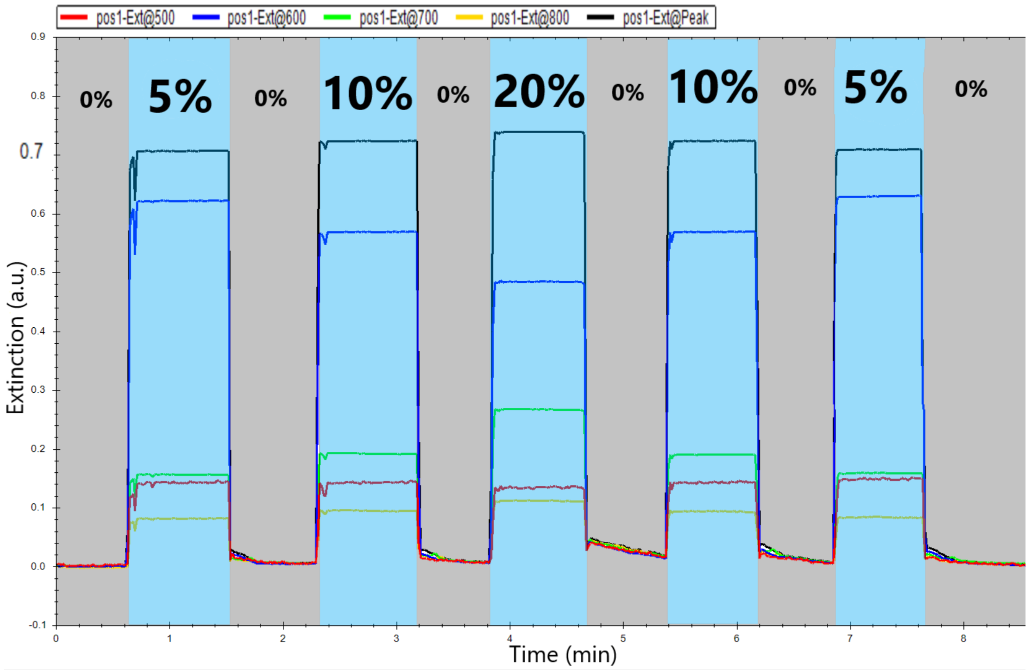

Figure 4.1: Light extinction as recorded in Insplorer software. Change in extinction as a function of time. The different colored lines correspond to the different wavelengths in nm shown in the legend. The specific fiber used for this test is a single sided fiber without fluoropolymer coating.

As we can see in figure 4.1, a sharp increase can be seen each time the fiber is submerged into the liquid and equilibrium is reached very fast, most of the bumps preceding the equilibrium is probably due to fiber movement or interactions with the tweezers used to break the surface tension. After submersion, a small slope can be observed until extinction levels drop back down to zero, this is probably due to residual liquid drying on the fiber. An effort was made to let the levels drop back down to zero extinction before proceeding, though it matters little, since it is washed away by the next solution and the amount is too small to significantly change the concentration of following solutions. Another clear trend when comparing the 600 nm and 700 nm spectra (blue and green plots in figure 4.1), is that the concentration has reversed effect on the extinctions. This is due to the maximum of the plasmonic peak being located in between these measurements, this phenomenon can be seen more clearly in figure 4.2, where some full spectra for one battery cycle is shown, the spectra are referenced to the beginning of the cycle, and each line represents the spectrum position in time, where the blue lines are the beginning of the cycle, and they become more and more red towards the end. For a more comprehensive explanation to the correlation in voltage signal see figures 4.10-4.12. For now we are primarily interested in the plasmonic peak, which would be located close to 750 nm in this case, at the inflection point. When the plasmon peak shifts, the greatest change in extinction may be seen in the inflection points of this peak. As can be seen in figure 4.2, these inflection points are found at 600 nm and 820 nm respectively, meaning that the peak is found in between these wavelengths. The peak is located where a minimal change in extinction can be seen, which is approximately at 750 nm.

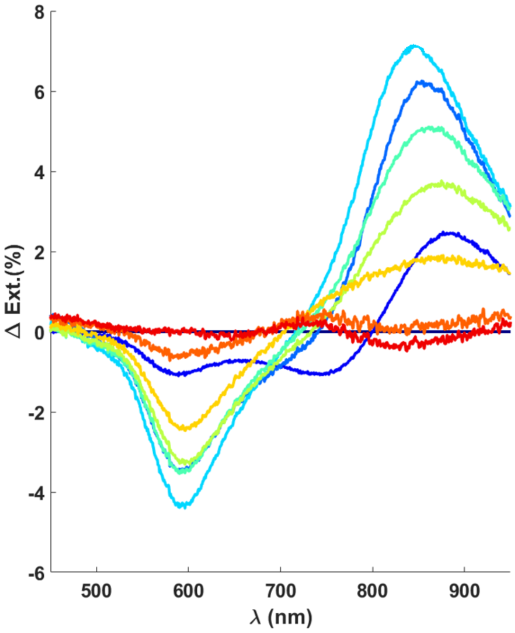

Figure 4.2: Some ΔExt. spectra for one complete battery cycle (charge/discharge), referenced at the beginning of the cycle.

To better understand the information we get from these spectra a few extra plots have been constructed. In figure 4.3 data from the same fiber as in figure 4.1 is shown where the transmission referenced to air vs wavelength is shown. The signal in air is simply taken during the first seconds of measurements before the fiber is dipped into solutions. One can see a clear overlap of the two curves in each concentration (apart from 20%, which only has one curve), suggesting that the signal is not significantly affected by previous measurements, considering the order in which the measurements were taken, as explained in section 3.2.2.1 (Bulk refractive index sensing (BRIS)). There is also a visible shift in $\Delta\lambda$, following the concentration gradient as explained in figure 2.1.

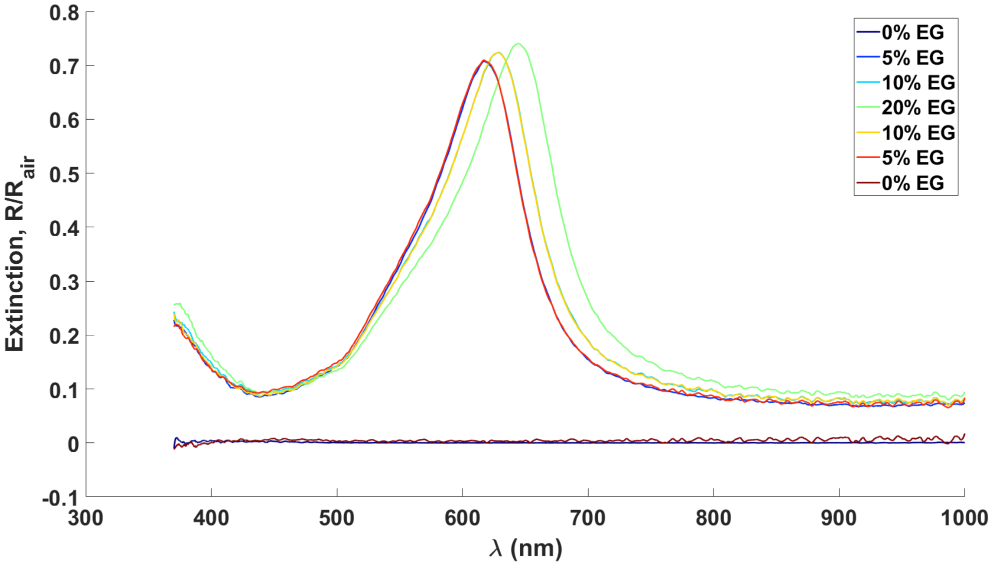

Figure 4.3: Extinction referenced to the signal in air as a function of wavelength, this is considered the plasmonic peak

To be able to quantify these result for easier comparison, three different values are extracted from the data, all of them are measures of BRIS. One is based on peak position, one on the optical center and the last on on percentage of extinction. The plot for the optical center BRIS determination can be seen in figure 3.3, and the BRIS value is the slope of the curve. The different results from the three determination methods can be seen in table 4.1, and based on the stability of the optical center determination, this was chosen as the preferred method, see section 3.2.1. Variance of the extinction method was 65000 with a standard deviation of 260.

Table 4.1: BRIS-values as calculated from different parameters.

Fiber (#)	**Fluoropolymer coated (y/n)**	**Single or double sided fiber**	**Peak Pos. (nm)**	**Optical Center (nm)**	**Extinction (%)**
1	n	Single	1886.8	1600.2	199.5
2	n	Single	2010	1452.8	376.7
3	n	Single	1651.5	1718.6	651.7
4	y	Single	1465.8	1046.4	155.5
5	y	Single	1361.9	885.5	188.0
6	y	Single	1237.2	911	108.6
7	n	Double	1796.6	1695.9	444.6
8	n	Double	1149.1	1540.3	477.8
9	n	Double	1613.2	1609.9	583.7
10	y	Double	826.1	1201.4	336.8
11	y	Double	1115.1	1244.2	-324.1
12	y	Double	717.6	1005.5	188.4
13	n	Double	1552.2	1293.8	258.5
14	n	Double	1254.5	962.5	269.4
15	n	Double	1379.6	1310.2	275.9
16	n	Double	1603.3	1170.3	486.1
17	y	Double	1076.6	1128.1	357.7
18	y	Double	1887.5	1014.7	202.1
19	y	Double	1031.3	1073.9	177.8
20	y	Double	1144.5	963.7	60.5

To easily visualize the variance of each data set and the difference between them, figure 4.4 was constructed. There are two sets of two sided fibers due to these being the fibres mainly used for *operando* testing. As can be seen in figure 4.4, the fluoropolymer coating has a negative impact on the sensitivity.

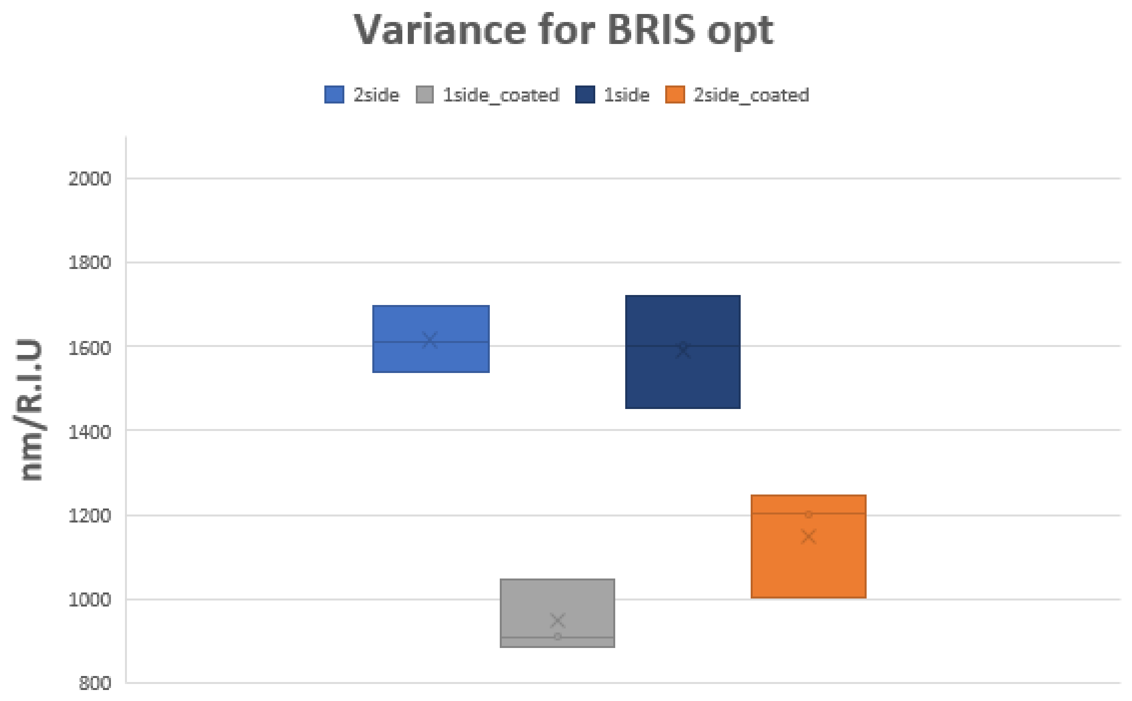

Figure 4.4: Variance in nm/R.I.U for the BRIS tested fibres. X marks the middle measurement, the line in each stack represent the median value, and for the last two measurements which contain four data-points instead of three, the extreme values are shown with the extending markers.

4.2 Electrochemical cycling

To get an understanding of how intrusive the fiber might be to the battery, a set of reference cells are cycled alongside the cells with optical sensors embedded into them. The two measures used to determine this are the capacity fade over cycles, which is calculated as mentioned in 3.2.1.1, and the efficiency. In figure 4.5 and figure 4.6 we can see the different plateaus corresponding to the different C-rates and we can see that the reference cells follow the same trends as the *operando* cells. To further be able to compare these results, four representative cells of each category have been tabulated in table 4.2.

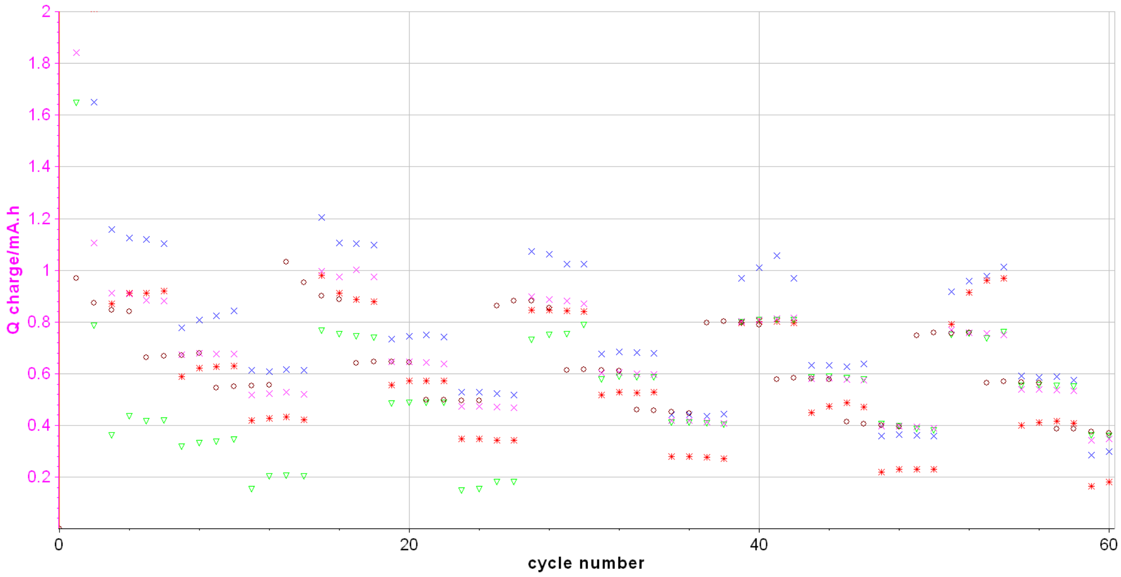

Figure 4.5: Capacity fade for the first 50 cycles for 5 reference cells, each datapoint corresponds to a cycle, they appear in groups of four following the cycling plan as seen in table 3.2

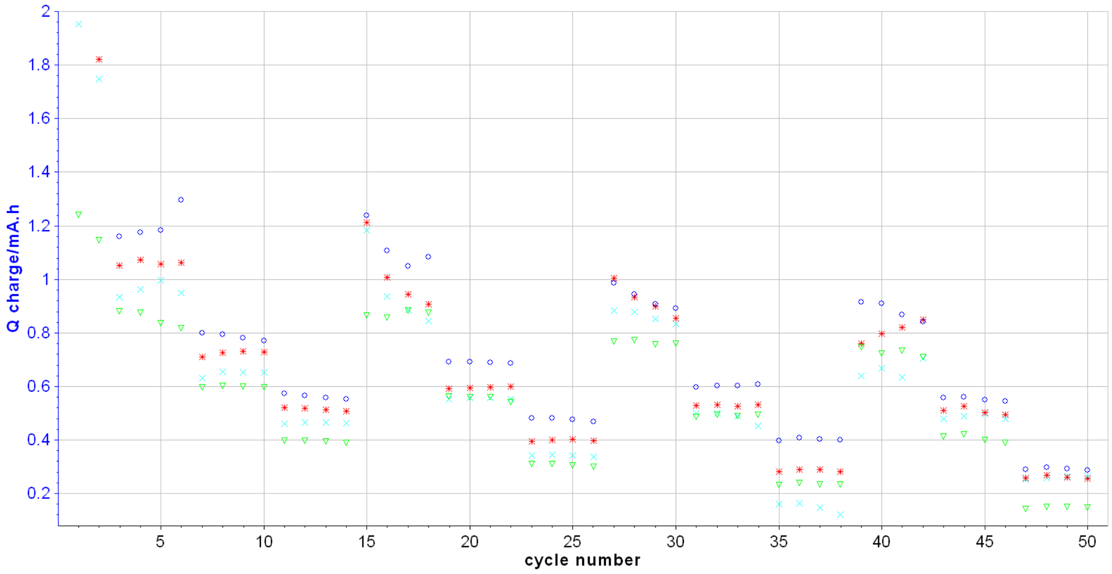

Figure 4.6: Capacity fade for the first 50 cycles for 4 *operando* cells, each datapoint corresponds to a cycle, they appear in groups of four following the cycling plan as seen in table 3.2

When comparing the values in table 4.2 the cells with optics show a trend of experiencing more capacity fade. This might be due to leakage at the drilled entry holes for the fiber, even though it has been glued with epoxy. It may also be that the electrolyte is contacting the epoxy and is interacting with it. And of course there are possible interactions with the fiber sensor that might affect this as well. It should also be mentioned that the 40 first cycles are the most turbulent ones, and that the trend might stabilize upon further cycling.

Table 4.2: Capacity fade over 40 cycles

Cell type	C/5 (%)	C/2 (%)	C/1 (%)
Reference	9	25	33
Reference	10	17	50
Reference	10	14	20
Reference	10	14	20
With optics	25	38	50
With optics	18	29	40
With optics	30	29	40
With optics	22	33	75

A second way for comparing the cells is to take a look at the Coulombic efficiency vs cycle number where the efficiency should be close to 100% across the cycles. In figure 4.7 we see the reference cells, and in figure 4.8 we see the cells containing the optical sensors. Notice that the outlying high and low values correspond to the changes in C-rates, but that the majority of the data points are right where they are supposed to be, at 100%. To further clarify this, figure 4.9 shows a reference cell (in blue) and a cell with optics (in red), where the coulombic efficiency stays stable for both cells during 80 cycles.

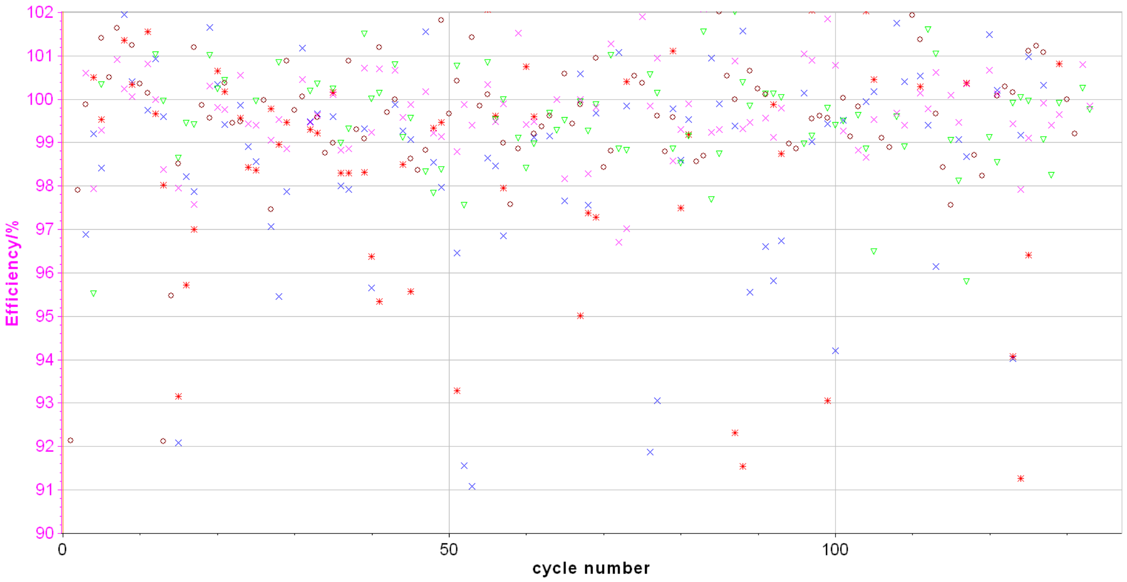

Figure 4.7: Coulombic efficiency vs cycle number for reference cells.

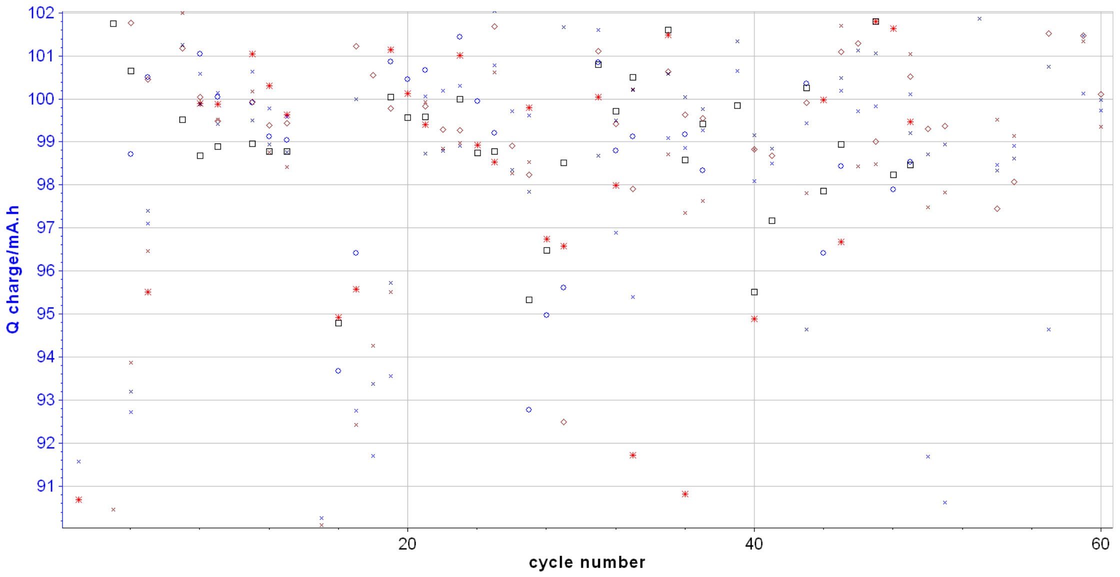

Figure 4.8: Coulombic efficiency vs cycle number for *operando* cells.

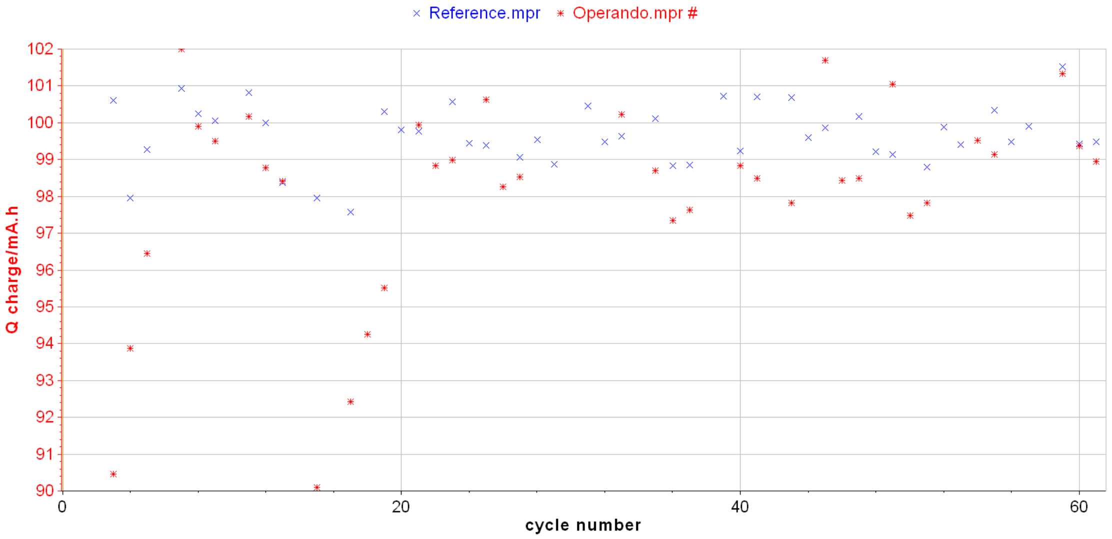

Figure 4.9: Coulombic efficiency vs cycle number for one cell with optics (red) and one reference cell (blue).

4.3 *Operando* measurements

The *operando* measurements have suffered from complications with the set up and the fragility of the fibers. Since every single step is carried out manually, many cells had defects which made the data unsuitable to collect. In the end three cells with the double sided fibers showed similar and reproducible trends. Six cells with single sided fibers are also presented, and the different fibers and their characteristics are listed in table 4.3. The last two single sided fibers (with sensing structure towards the anode) are included mainly to provide a better overview of the system and a wider base for discussion. They are nevertheless the only two cells of their kind, and not the three most stable and representative as is the case with the other two sets, and therefore do not carry the same weight and significance in the conclusions.

Table 4.3: Fiber number and characteristics

Fiber number	1 or 2-sided	Coated (y/n)	Orientation
1	2	yes	-
2	2	yes	-
3	2	yes	-
4	1	no	Separator
5	1	no	Separator
6	1	no	Separator
7	1	yes	Anode
8	1	yes	Anode

To analyse the spectrum as efficiently as possible, it is of great importance to find the signal which contains the most relevant information. In this case it would be the spectrum with a wavelength triggering the maximal response from the plasmonic resonance. To investigate this figures 4.10-4.12 have been produced to show how the spectrum responds during cycling. In figure 4.10 the plasmonic peak is found close to 750 nm, furthermore, the response at higher wavelengths shows greater amplitude compared to wavelengths below the plasmonic peak. In figure 4.13 the effect of this can be clearly seen in the optical signals. In the light of this distribution, closer analysis is made using the ΔExt. at 850 nm.

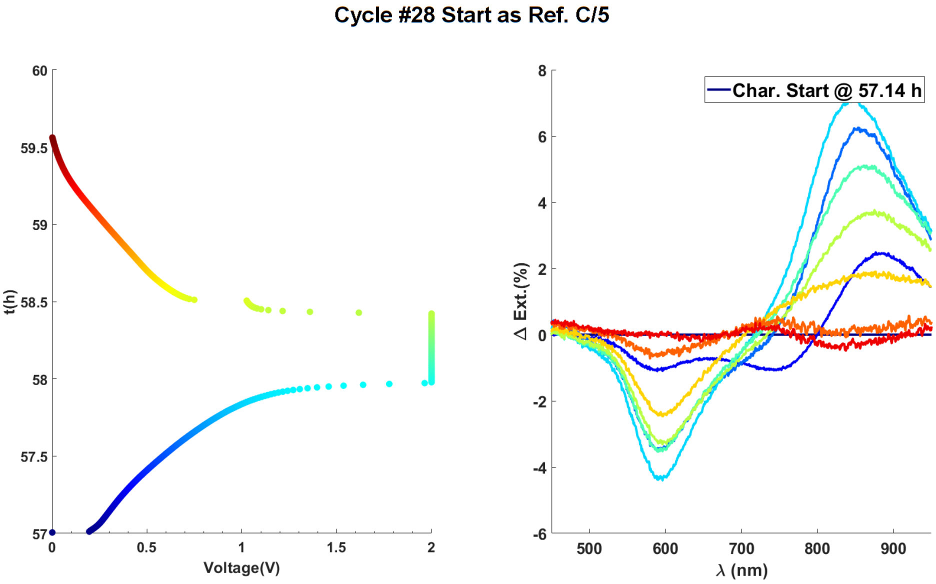

Figure 4.10: Voltage data compared to the ΔExt. spectra at a few timestamps for cell 1 (2-sided, coated). The time correlation between the plots is illustrated by the color of the graph.

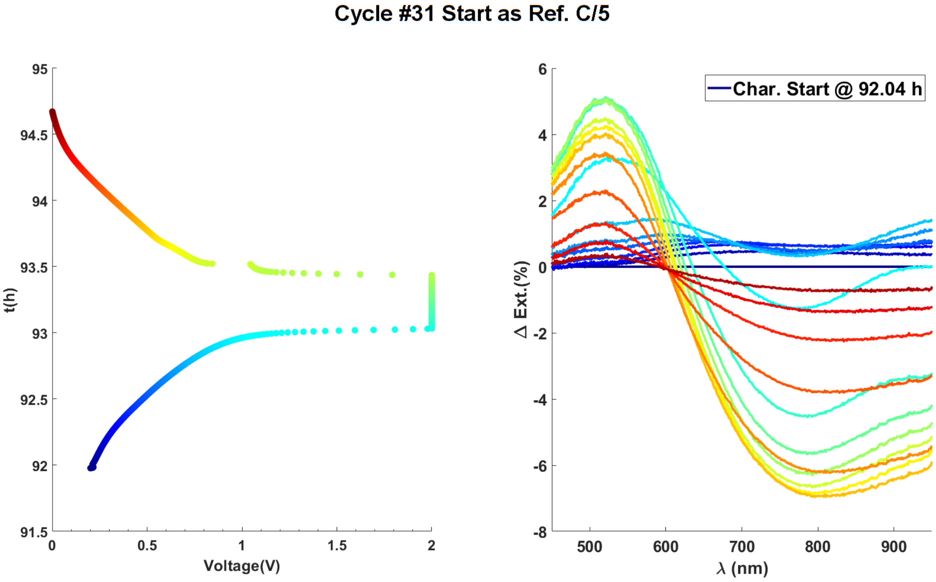

Figure 4.11: Voltage data compared to the ΔExt. spectra at a few timestamps for cell 6 (1-sided, uncoated, towards separator). The time correlation between the plots is illustrated by the color of the graph.

Figure 4.11 is showing cell 6, which has no fluoropolymer coating and the sensing structure towards the separator. Compared to cell 1 in figure 4.10 the plasmonic peak has shifted to approximately 650 nm. This can be due to a number of reasons, firstly the lack of coating obviously changes the refractive index in the fibers immediate surrounding, a theory that might be discarded due to the similarities to figure 4.12. Cell 8 as seen in figure 4.12 has the fluoropolymer coating, which is why we would rather suspect the sidedness of the fiber to cause the change in plasmonic peak position and not the coating. However, the single sided cells with fibers oriented towards the anode make up a poor population size, combined with the data not showing as clear trends as the other cells, it is a poor foundation for conclusions. As mentioned, a possibility for the change in plasmonic peak position between the double and single sided fibers is the interaction of light between the two sides, where the double sided fiber due to the larger sensing area might sense multiple chemical events surrounding it, leading to extinction at different wavelengths. A third possibility is that the sensing structure towards the separator senses little to no change. This would be expected due to no chemical change in the structure of the separator as opposed to the anode material. The sensing would then in this case be done by the naked fiber, acting like an evanescent wave sensor as mentioned in section 2.3 (Fiber optic sensors).

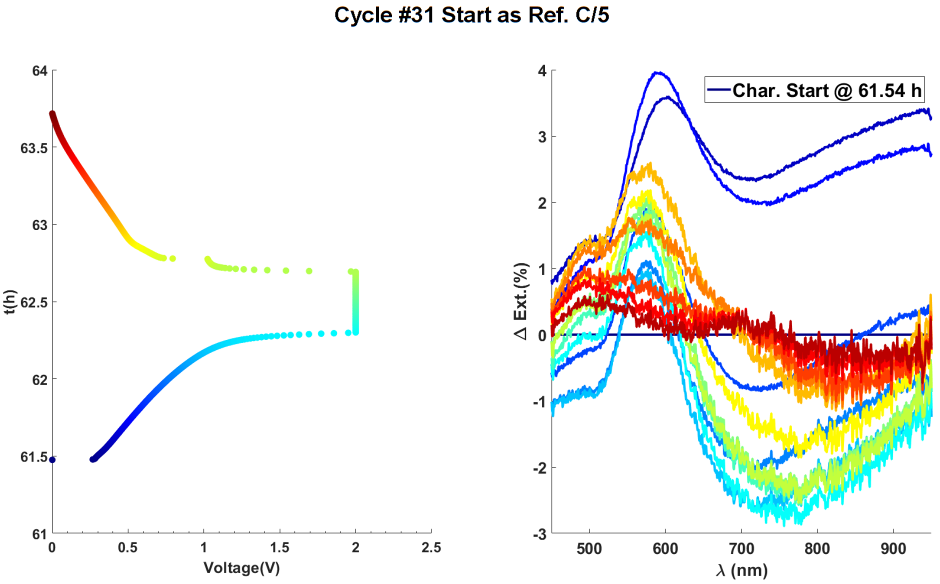

Figure 4.12: Voltage data compared to the ΔExt. spectra at a few timestamps for cell 8 (1-sided, coated, towards anode). The time correlation between the plots is illustrated by the color of the graph.

Even though the data in figure 4.12 does not show any overwhelmingly clear signal, the plasmonic peak remains close to 650 nm, suggesting that the coating of the fiber has less significance to the results than the single or double sidedness of the sensor.

In figures 4.13-4.15, we see one representative cell from each category and the data collected for them. The other cells and their graphs as seen in table 4.3, can be found in Appendix 1 as figures A.1-A.5. Electrochemically, the voltage and current is recorded and then via Matlab matched to the optical output, which is a spectrum recorded in intervals. In theses overview figures the wavelengths 650 nm and 850 nm were chosen to represent the entire picture, this is due to their favourable position in correlation to the plasmonic peak. The extinction is presented as ΔExt. with the reference is taken at the beginning of cycling.

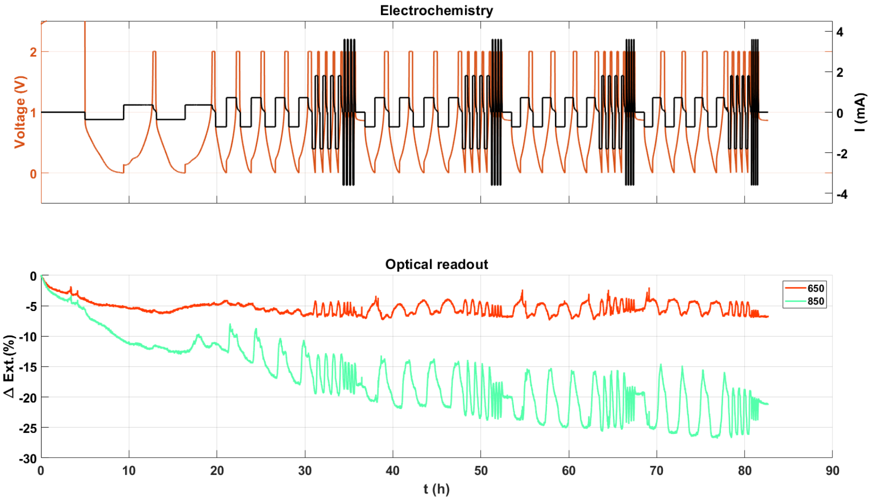

Figure 4.13: An overview of the different parameters measured during *operando* measurements for fiber 1 (2-sided, coated). 650 and 850 nm were chosen as best wavelengths according to figure 4.10.

Before any deeper analysis of the signal, some features of the graphs ought to be more thoroughly examined, in figure 4.13 both optical signals show an increase in amplitude as time progresses, the 850 nm signal more so than the 650 nm one. Furthermore, a slight drift in the signal can be observed, again more prominently for the 850 nm signal.

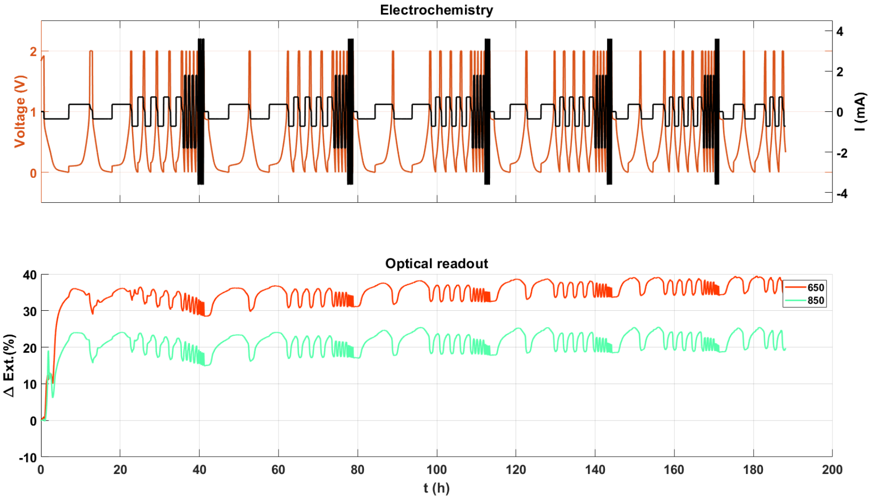

Figure 4.14: An overview of the different parameters measured during *operando* measurements for fiber 4 (1-sided, uncoated, towards separator). 650 and 850 nm were chosen as representative wavelengths according to figure 4.10.

In figure 4.14, the fiber is single sided and oriented towards the separator, the drift and amplitude increase as seen in 4.13 is minimal here. At this point in the measurements the cycling regime has changed to the one found in table 3.2. For further information on the change in cycling regime see section 3.2.1 (Cell set-up and electrochemical cycling).

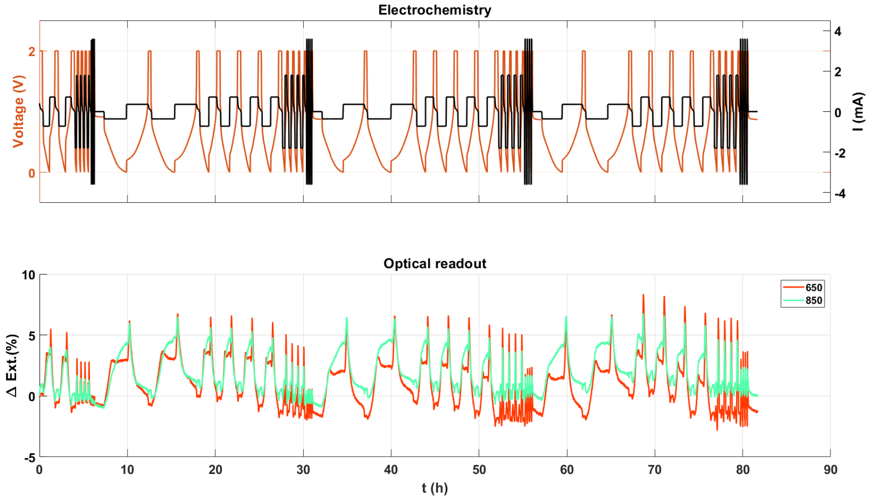

Figure 4.15: An overview of the different parameters measured during *operando* measurements for fiber 7 (1-sided, coated, towards anode). 650 and 850 nm were chosen as representative wavelengths according to figure 4.10.

The measurement for cell 7 was interrupted due to computer issues, and therefore the graph in figure 4.15 is starting in between cycles. Since the majority of the measurement was intact and uninterrupted during this period, it was chosen to represent the entire cycling of the cell. Some drift and signal amplification can be seen.

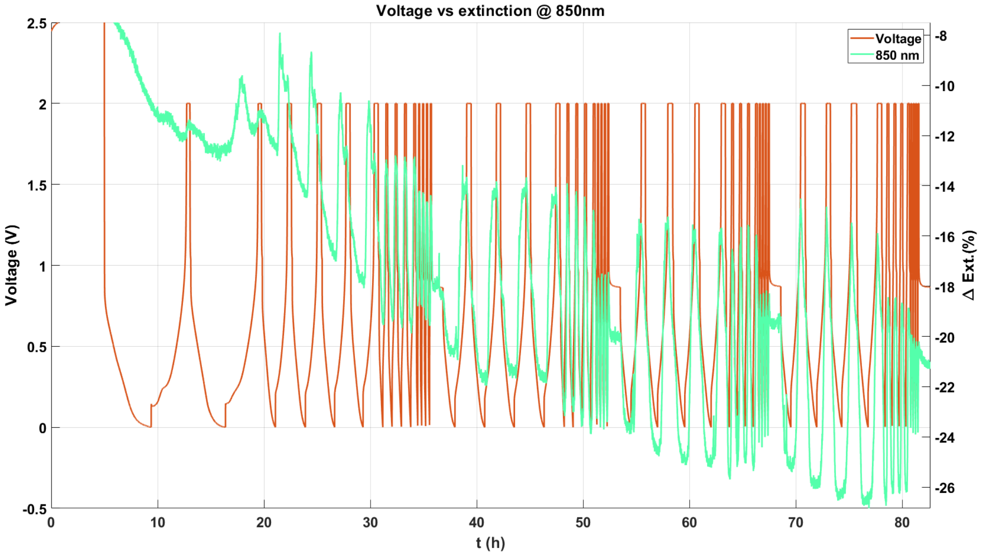

Figure 4.16: Voltage signal and ΔExt. vs time for cell 1 (2-sided, coated).

Having established that 850 nm produces a high amplitude in ΔExt. for all the different sets, a few more figures were produced to get a better sense of signal drift and correlation between the voltage and optical signals. These trends can be seen in figures 4.16-4.21, and like before, the cells not shown here are listed in the appendix in figures A.6-A.15. The seemingly inverted signal which is clearly visible when comparing figure 4.17 and 4.19, is due to the plasmonic peak shifting in different directions. measurement in the light of the plasmonic peak shift, hence the raw signal is much the same between the two figures.

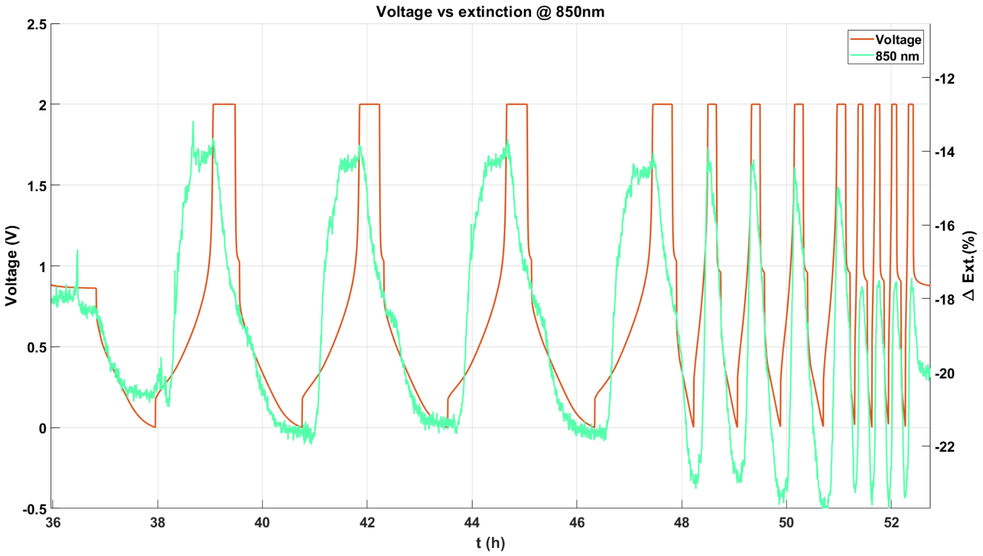

Figure 4.17: Voltage signal and ΔExt. vs time for cell 1 (2-sided, coated).

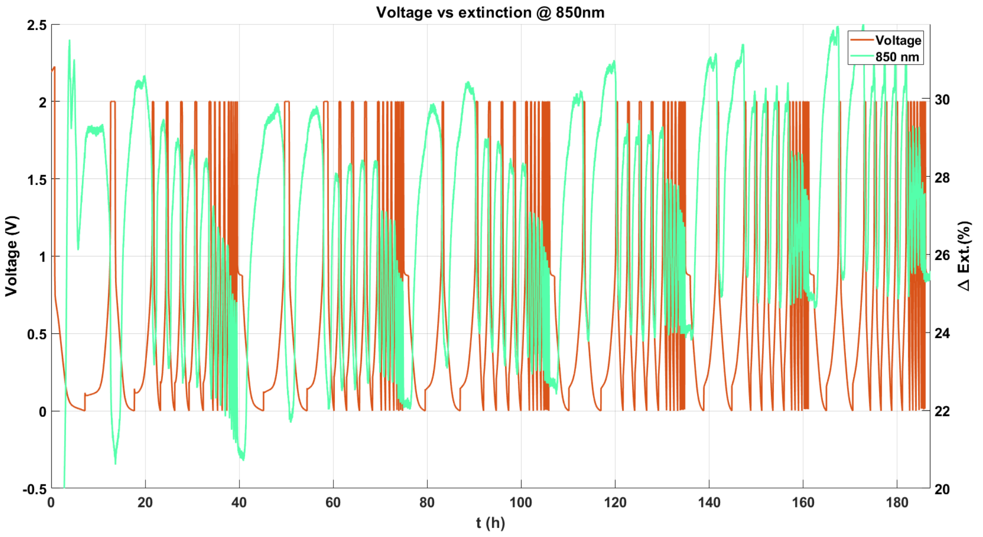

Figure 4.18: Voltage signal and ΔExt. vs time for cell 6 (1-sided, uncoated, towards separator).

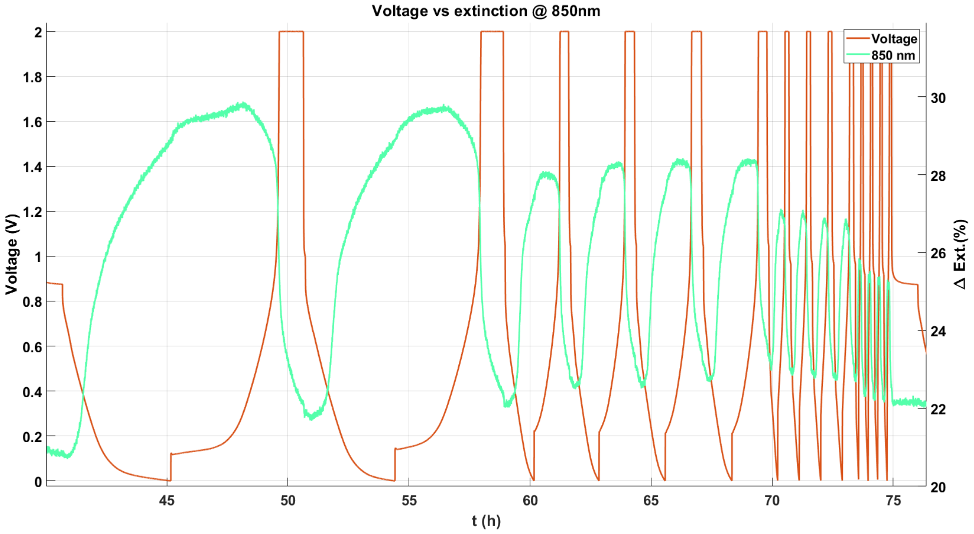

Figure 4.19: Voltage signal and ΔExt. vs time for cell 6 (1-sided, uncoated, towards separator).

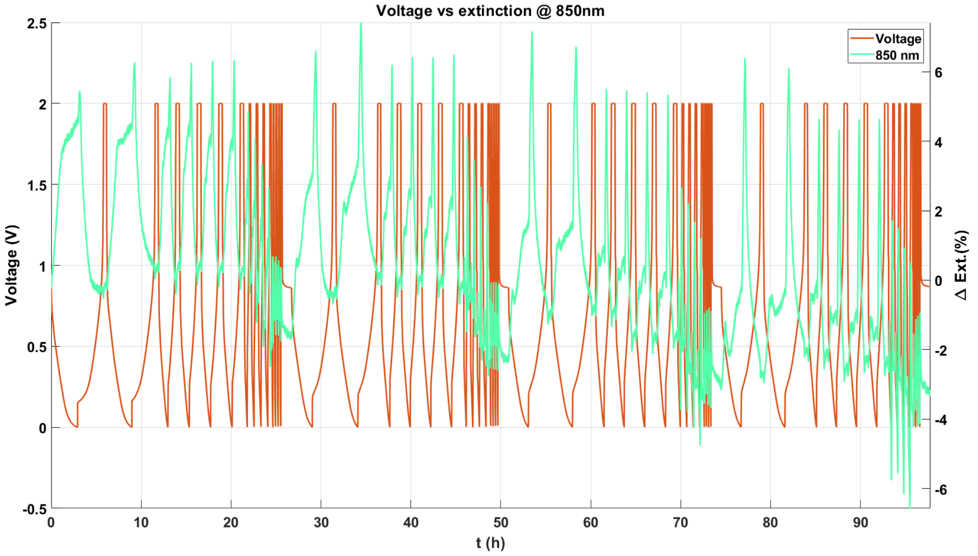

Figure 4.20: Voltage signal and ΔExt. vs time for cell 8 (1-sided, coated, towards anode).

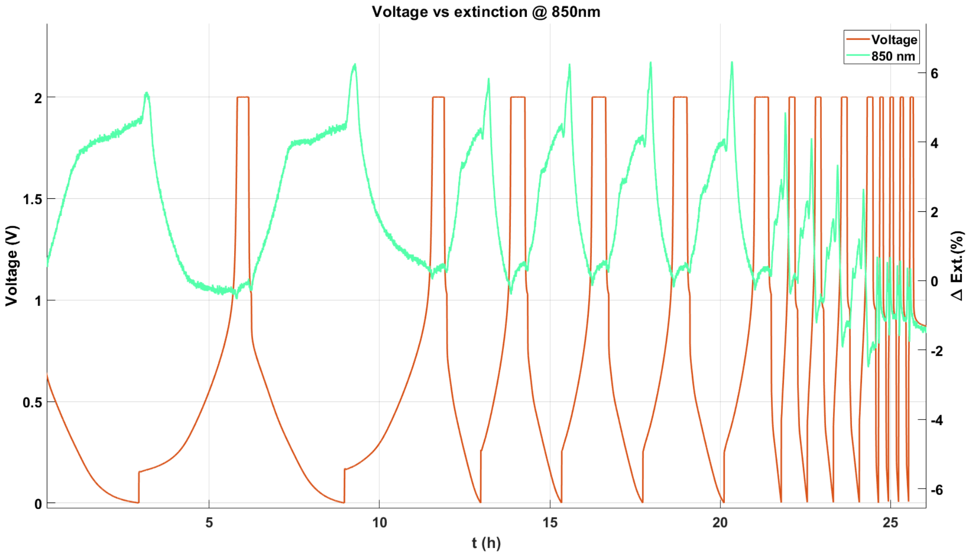

Figure 4.21: Voltage signal and ΔExt. vs time for cell 8 (1-sided, coated, towards anode).

The inverted readout between the fibers depending on sidedness is further clarified in figures 4.22-4.25, where figures 4.22 and 4.23 show cell 3:s voltage and ΔExt. vs DoD at C/10 and C/5 respectively. Comparing this to the corresponding plots for cell 4 in figures 4.24 and 4.25, one can see the trend of the optical signal, though inverted, remains the same. Every ΔExt. is referenced to the start of the discharge, meaning that permanent changes such as SEI layers, will be referenced out for following cycles.

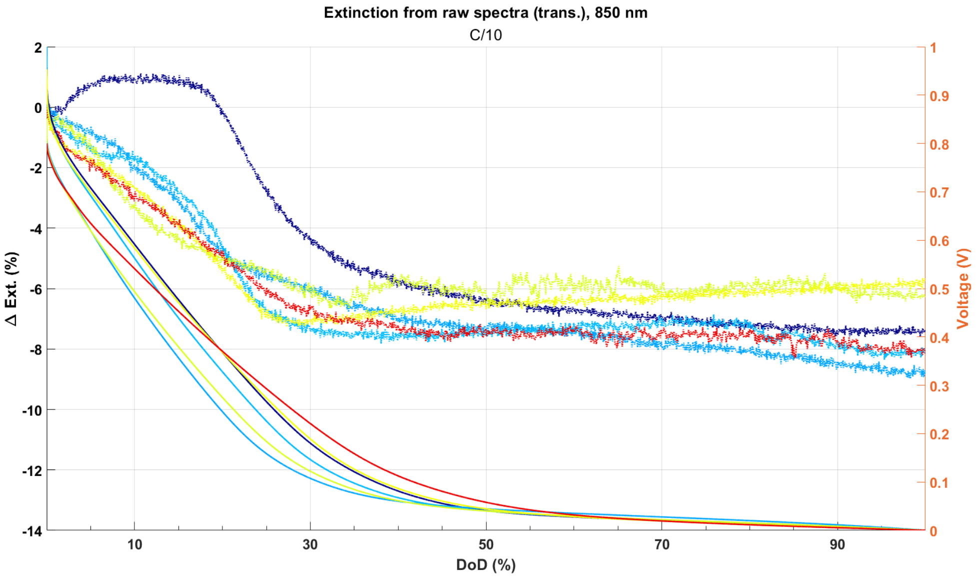

Figure 4.22: A collection of signal responses from the discharge cycles at C/10, voltage and ΔExt. vs DoD. The colors match the optical responses to the voltage signal of corresponding cycle, and also show a gradient where early cycles are deep blue and later cycles turn to red. This graph is for cell 3 (2-sided, coated).

Both figure 4.22 and 4.24 contain the first cycle of the cycling regime, and in both cases the first optical signal response deviates from the rest of the cycles. This is most likely due to the SEI formation process, further proving the sensors ability to sense change in chemical composition. Every ΔExt. in figures 4.22-4.25, is referenced to the start of the discharge, meaning that permanent changes to chemical composition, such as a SEI layer, become hidden in the signal after complete formation.

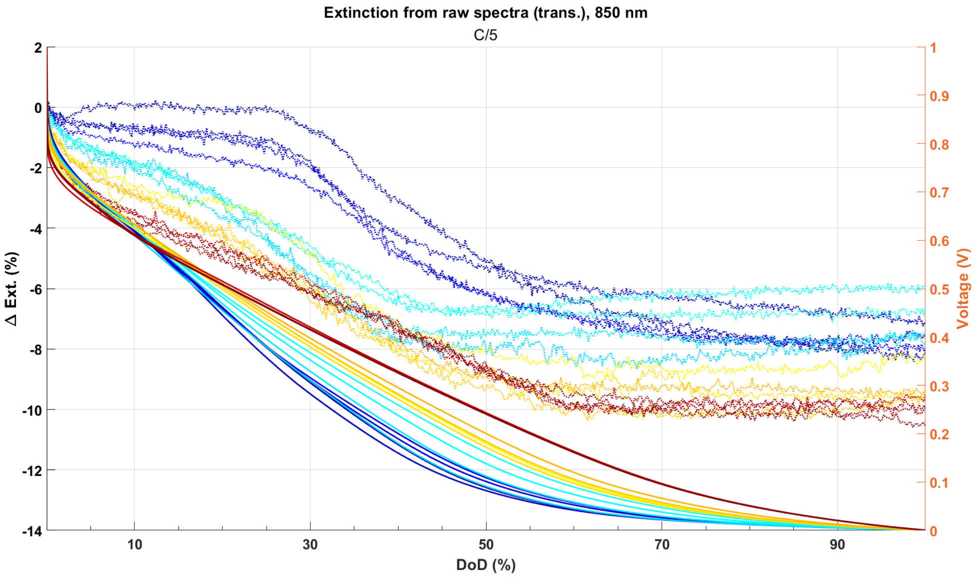

Figure 4.23: A collection of signal responses from the discharge cycles at C/5, voltage and ΔExt. vs DoD. The colors match the optical responses to the voltage signal of corresponding cycle, and also show a gradient where early cycles are deep blue and later cycles turn to red. This graph is for cell 3 (2-sided, coated).

The voltage signal displays a trend where the plateau region diminishes over time, most clearly seen in figure 4.24. According to Sun et al. the Na-ion storage mechanism follows the adsorption-intercalation model, and states that the contribution from intercalation to the overall capacity is seen in the plateau region. The reason for the intercalation being associated with the plateau region is the slow kinetics involved in reaching the areas suitable for intercalation as well as the intercalation itself. Considering the cells in this study and the very high C-rates they experienced in intervals, it is reasonable to assume some capacity fade due to ions left in the HC structure, more specifically, one would expect to see a decrease in the plateau region. Since the kinetics in this region are slower, it would be here the main part of ions are trapped, leading to a "poisoning" of the anode.

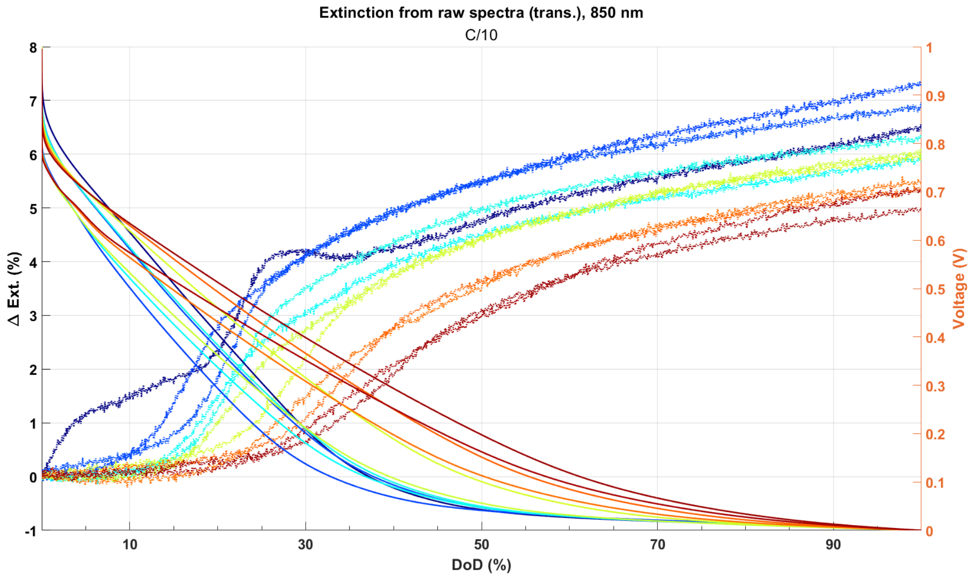

Figure 4.24: A collection of signal responses from the discharge cycles at C/10, voltage and ΔExt. vs DoD. The colors match the optical responses to the voltage signal of corresponding cycle, and also show a gradient where early cycles are deep blue and later cycles turn to red. This graph is for cell 4 (1-sided, uncoated, towards separator).

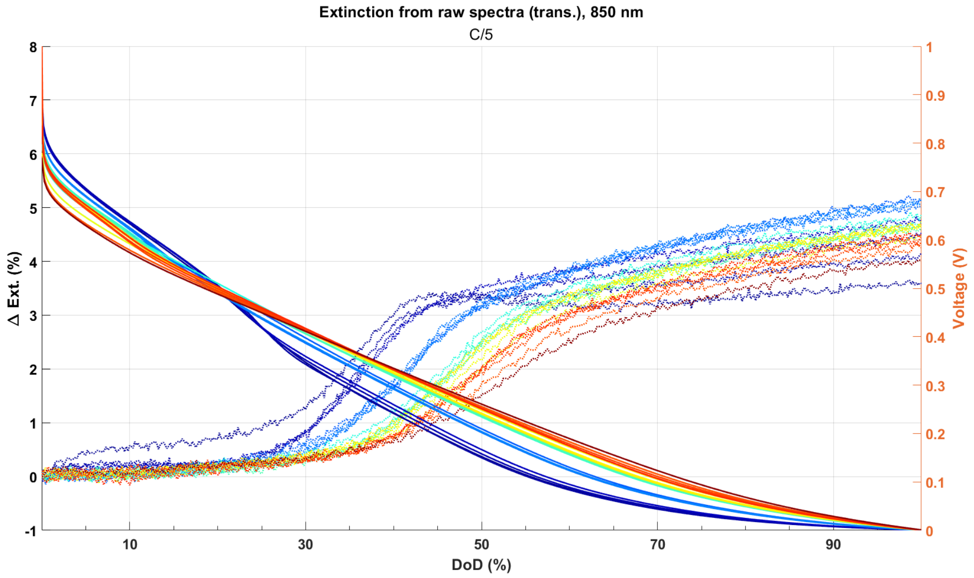

Figure 4.25: A collection of signal responses from the discharge cycles at C/5, voltage and ΔExt. vs DoD. The colors match the optical responses to the voltage signal of corresponding cycle, and also show a gradient where early cycles are deep blue and later cycles turn to red. This graph is for cell 4 (1-sided, uncoated, towards separator).

5

Conclusions

Since the data collected are insufficient to enable us to propose a Na-ion storage mechanism, most of the analysis and discussion are on a qualitative level.

As the plasmons are sensitive to many phenomena, sensing complex systems, will need to rely on correlations. Using different sensors and protocols and other probes as references. In tandem with other methods that possess greater specificity, such as Raman and *in situ* NMR spectroscopy, NPS might be a valuable tool in elucidating the Na-ion storage mechanism in HC.

The sensors clearly do, however, sense internal events in the battery cells, and can reliably measure these in real time. The measurements are reproducible and sensitive to the charge and discharge cycles as well as SEI formation.

5.1 Improvements to the method

The sensor holding implement for BRIS measurements might be improved to allow for measurements in a fashion more closely resembling the way they are oriented during *operando* measurements i.e. without a bend. How to properly do this still needs to be explored, although it is most likely a very low priority due to the decent results gathered from the bent setup.

Having the batteries cycle in a climate controlled chamber without light sources would greatly decrease the number of factors potentially affecting the measurements. The room in which the measurements were conducted was open and other people were working at adjacent surfaces, which means further risk of drafts or bumps that might shake the fibers, which they are quite sensitive to.

5.2 Further experiments

The test most notably lacking from the lineup of tests is maybe the one with a bare fiber. Using this measurement as a reference one might get a better understanding of how and why the single sided fibers differ from the double sided ones, which could be very valuable. Furthermore, completing the tests with a matrix of all the different configurations, and have more tests to reliably produce statistically sound theories would be of great benefit.

There is significant difference between the fiber types measured, suggesting that different setups might be used to gain different insights to the system. In this study the greatest change in position of the fiber was achieved by orienting the gold structure towards the separator or the anode, although there might be information gained on how ion transport is perceived by the fiber if it was placed on the other side of the separator (between the separator and the cathode). In this position we would not expect any chemical change after formation cycles, and if it indeed does not sense anything in this position, a double fiber setup might be used where the second fiber could act as an internal reference sensor.

Bibliography

[1] Huilin Pan, Yong-Sheng Hu, and Liquan Chen. "Room-temperature stationary sodium-ion batteries for large-scale electric energy storage". In: *Energy Environ. Sci.* 6 (8 2013), pp. 2338–2360. DOI: `10.1039/C3EE40847G`. URL: `http://dx.doi.org/10.1039/C3EE40847G`.

[2] James Robinson et al. "Microstructural Analysis of the Effects of Thermal Runaway on Li-Ion and Na-Ion Battery Electrodes". In: *Journal of Electrochemical Energy Conversion and Storage* 15 (Nov. 2017). DOI: `10.1115/1.4038518`.

[3] Kei Kubota and Shinichi Komaba. "Review—Practical Issues and Future Perspective for Na-Ion Batteries". In: *Journal of The Electrochemical Society* 162.14 (2015), A2538–A2550. ISSN: 0013-4651. DOI: `10.1149/2.0151514jes`.

[4] Samuel Roberts and Emma Kendrick. "The re-emergence of sodium ion batteries: Testing, processing, and manufacturability". In: *Nanotechnology, Science and Applications* 11 (2018), pp. 23–33. ISSN: 11778903. DOI: `10.2147/NSA.S146365`.

[5] James B. Robinson et al. "Multiscale tomographic analysis of the thermal failure of Na-Ion batteries". In: *Journal of Power Sources* 400.July (2018), pp. 360–368. ISSN: 03787753. DOI: `10.1016/j.jpowsour.2018.07.098`. URL: `https://doi.org/10.1016/j.jpowsour.2018.07.098`.

[6] Michael D. Slater et al. "Sodium-ion batteries". In: *Advanced Functional Materials* 23.8 (2013), pp. 947–958. ISSN: 16163028. DOI: `10.1002/adfm.201200691`.

[7] Katherine Smith et al. "Novel High Energy Density Sodium Layered Oxide Cathode Materials: from Material to Cells". In: *ECS Transactions* 75.22 (2017), pp. 13–24. ISSN: 1938-6737. DOI: `10.1149/07522.0013ecst`.

[8] Chong Liu et al. "Lithium Extraction from Seawater through Pulsed Electrochemical Intercalation". In: *Joule* 4.7 (2020), pp. 1459–1469. ISSN: 25424351. DOI: `10.1016/j.joule.2020.05.017`. URL: `https://doi.org/10.1016/j.joule.2020.05.017`.

[9] K. M. Abraham. "How Comparable Are Sodium-Ion Batteries to Lithium-Ion Counterparts?" In: *ACS Energy Letters* 5.11 (2020), pp. 3544–3547. ISSN: 23808195. DOI: `10.1021/acsenergylett.0c02181`.

[10] "In Progress in the Commercialization of Faradion's Na-ion Battery Technology". In: 2017.

[11] Nuria Tapia-ruiz et al. “Journal of Physics : Energy OPEN ACCESS 2021 roadmap for sodium-ion batteries”. In: *Journal of Physics: Energy* 3 (2021), p. 031503.

[12] Laure Cailloce. *A battery revolution in motion.* https://news.cnrs.fr/articles/a-battery-revolution-in-motion. Accessed: 2021-11-08. 2015.

[13] Julia S. Weaving et al. “Elucidating the Sodiation Mechanism in Hard Carbon by Operando Raman Spectroscopy”. In: *ACS Applied Energy Materials* (Aug. 2020), acsaem.0c00867. ISSN: 2574-0962. DOI: `10.1021/acsaem.0c00867`. URL: `https://pubs.acs.org/doi/10.1021/acsaem.0c00867`.

[14] M Anji Reddy et al. “Insight into Sodium Insertion and the Storage Mechanism in Hard Carbon”. In: *ACS Energy Letters* 3 (2018), pp. 1–8. ISSN: 2380-8195. DOI: `10.1021/acsenergylett.8b01761`. URL: `http://pubs.acs.org/doi/10.1021/acsenergylett.8b01761`.

[15] Damien Saurel et al. “From Charge Storage Mechanism to Performance: A Roadmap toward High Specific Energy Sodium-Ion Batteries through Carbon Anode Optimization”. In: *Advanced Energy Materials* 8.17 (2018), pp. 1–33. ISSN: 16146840. DOI: `10.1002/aenm.201703268`.

[16] M. Anji Reddy et al. “Insight into Sodium Insertion and the Storage Mechanism in Hard Carbon”. In: *ACS Energy Letters* 3.12 (Dec. 2018), pp. 2851–2857. ISSN: 2380-8195. DOI: `10.1021/acsenergylett.8b01761`. URL: `http://pubs.acs.org/doi/10.1021/acsenergylett.8b01761`.

[17] Zelang Jian et al. “Insights on the Mechanism of Na-Ion Storage in Soft Carbon Anode”. In: *Chemistry of Materials* 29.5 (Mar. 2017), pp. 2314–2320. ISSN: 0897-4756. DOI: `10.1021/acs.chemmater.6b05474`. URL: `https://pubs.acs.org/doi/10.1021/acs.chemmater.6b05474`.

[18] Shinichi Komaba et al. “Electrochemical Na Insertion and Solid Electrolyte Interphase for Hard-Carbon Electrodes and Application to Na-Ion Batteries”. en. In: *Advanced Functional Materials* 21.20 (Oct. 2011), pp. 3859–3867. ISSN: 1616301X. DOI: `10.1002/adfm.201100854`. URL: `http://doi.wiley.com/10.1002/adfm.201100854`.

[19] Xiuyi Lin et al. “Advanced lignin-derived hard carbon for Na-ion batteries and a comparison with Li and K ion storage”. In: *Carbon* 157 (Feb. 2020), pp. 316–323. ISSN: 00086223. DOI: `10.1016/j.carbon.2019.10.045`.

[20] Aurora Gomez-Martin et al. “Correlation of Structure and Performance of Hard Carbons as Anodes for Sodium Ion Batteries”. In: *Chemistry of Materials* 31.18 (Sept. 2019), pp. 7288–7299. ISSN: 0897-4756. DOI: `10.1021/acs.chemmater.9b01768`. URL: `https://pubs.acs.org/doi/10.1021/acs.chemmater.9b01768`.

[21] Chenglong Zhao et al. “Novel Methods for Sodium-Ion Battery Materials”. In: *Small Methods* 1.5 (2017), p. 1600063. ISSN: 23669608. DOI: `10.1002/smtd.201600063`. URL: `http://doi.wiley.com/10.1002/smtd.201600063`.

[22] Ning Sun et al. “Extended “Adsorption–Insertion” Model: A New Insight into the Sodium Storage Mechanism of Hard Carbons”. In: *Advanced Energy Materials* (July 2019), p. 1901351. ISSN: 1614-6832. DOI: `10.1002/aenm.201901351`. URL: `https://onlinelibrary.wiley.com/doi/abs/10.1002/aenm.201901351`.

[23] Biwei Xiao, Teófilo Rojo, and Xiaolin Li. "Hard Carbon as Sodium-Ion Battery Anodes: Progress and Challenges". In: *ChemSusChem* 12.1 (2019), pp. 133–144. ISSN: 1864564X. DOI: `10.1002/cssc.201801879`.

[24] Cristina Nita et al. "Hard carbon derived from coconut shells, walnut shells, and corn silk biomass waste exhibiting high capacity for Na-ion batteries". In: *Journal of Energy Chemistry* 58 (2021), pp. 207–218. ISSN: 20954956. DOI: `10.1016/j.jechem.2020.08.065`. URL: `https://doi.org/10.1016/j.jechem.2020.08.065`.

[25] Elmira Memarzadeh et al. "<High Density Sodium and Lithium Ion Battery Anodes from Banana Peels.pdf>". In: ().

[26] Yang Duan Su et al. "Fiber optic sensing technologies for battery management systems and energy storage applications". In: *Sensors (Switzerland)* 21.4 (2021), pp. 1–36. ISSN: 14248220. DOI: `10.3390/s21041397`.

[27] Robert R. Richardson, Peter T. Ireland, and David A. Howey. "Battery internal temperature estimation by combined impedance and surface temperature measurement". In: *Journal of Power Sources* 265 (2014), pp. 254–261. ISSN: 03787753. DOI: `10.1016/j.jpowsour.2014.04.129`. URL: `http://dx.doi.org/10.1016/j.jpowsour.2014.04.129`.

[28] H. P.G.J. Beelen et al. "A comparison and accuracy analysis of impedance-based temperature estimation methods for Li-ion batteries". In: *Applied Energy* 175 (2016), pp. 128–140. ISSN: 03062619. DOI: `10.1016/j.apenergy.2016.04.103`. URL: `http://dx.doi.org/10.1016/j.apenergy.2016.04.103`.

[29] Jinli Zhu et al. "Facile photochemical synthesis of ZnWO4/Ag yolk-shell microspheres with enhanced visible-light photocatalytic activity". In: *Materials Letters* 190 (2017), pp. 60–63. ISSN: 18734979. DOI: `10.1016/j.matlet.2016.12.056`. URL: `http://dx.doi.org/10.1016/j.matlet.2016.12.056`.

[30] Mahaveer K Jain et al. "Magnetoacoustic remote query". In: (2000).

[31] M. K. Jain et al. "Measurement of temperature and liquid viscosity using wireless magneto-acoustic/magneto-optical sensors". In: *IEEE Transactions on Magnetics* 37.4 (2001), pp. 2767–2769. ISSN: 00189464. DOI: `10.1109/20.951301`.

[32] Craig A. Grimes and Dimitris Kouzoudis. "Remote query measurement of pressure, fluid-flow velocity, and humidity using magnetoelastic thick-film sensors". In: *Sensors and Actuators, A: Physical* 84.3 (2000), pp. 205–212. ISSN: 09244247. DOI: `10.1016/S0924-4247(00)00306-X`.

[33] Zhongbao Wei et al. "Future smart battery and management: Advanced sensing from external to embedded multi-dimensional measurement". In: *Journal of Power Sources* 489.January (2021), p. 229462. ISSN: 03787753. DOI: `10.1016/j.jpowsour.2021.229462`. URL: `https://doi.org/10.1016/j.jpowsour.2021.229462`.

[34] Royal Society. "Crystallite growth in graphitizing and non-graphitizing carbons". In: *Proceedings of the Royal Society of London. Series A. Mathematical and Physical Sciences* 209.1097 (1951), pp. 196–218. ISSN: 0080-4630. DOI: `10.1098/rspa.1951.0197`.

[35] Martin Z. Bazant. “Editorial Overview: Fundamental and Theoretical ElectrochemistryAdvances in the theory of electrochemical interfaces”. In: *Current Opinion in Electrochemistry* 13 (2019), A1–A4. ISSN: 24519111. DOI: `10.1016/j.coelec.2019.02.008`. URL: `https://doi.org/10.1016/j.coelec.2019.02.008`.

[36] P. Kurzweil. “Gaston Planté and his invention of the lead-acid battery-The genesis of the first practical rechargeable battery”. In: *Journal of Power Sources* 195.14 (2010), pp. 4424–4434. ISSN: 03787753. DOI: `10.1016/j.jpowsour.2009.12.126`.

[37] Matthew Li et al. “30 Years of Lithium-Ion Batteries”. In: *Advanced Materials* 30.33 (2018), pp. 1–24. ISSN: 15214095. DOI: `10.1002/adma.201800561`.

[38] Mohammed Yekini Suberu, Mohd Wazir Mustafa, and Nouruddeen Bashir. “Energy storage systems for renewable energy power sector integration and mitigation of intermittency”. In: *Renewable and Sustainable Energy Reviews* 35 (2014), pp. 499–514. ISSN: 13640321. DOI: `10.1016/j.rser.2014.04.009`. URL: `http://dx.doi.org/10.1016/j.rser.2014.04.009`.

[39] Jasper Biemolt et al. “Beyond Lithium-Based Batteries”. In: (2020), pp. 1–31.

[40] Ibrahim Dincer and Dogan Erdemir. “Chapter 1 - Fundamentals and Concepts”. In: *Heat Storage Systems for Buildings*. Ed. by Ibrahim Dincer and Dogan Erdemir. Elsevier, 2021, pp. 1–35. ISBN: 978-0-12-823572-0. DOI: `https://doi.org/10.1016/B978-0-12-823572-0.00007-2`. URL: `https://www.sciencedirect.com/science/article/pii/B9780128235720000072`.

[41] Farschad Torabi and Pouria Ahmadi. “Chapter 1 - Battery technologies”. In: *Simulation of Battery Systems*. Ed. by Farschad Torabi and Pouria Ahmadi. Academic Press, 2020, pp. 1–54. ISBN: 978-0-12-816212-5. DOI: `https://doi.org/10.1016/B978-0-12-816212-5.00005-2`. URL: `https://www.sciencedirect.com/science/article/pii/B9780128162125000052`.

[42] Joanne L Murray. “The Al — Na (Aluminum-Sodium) system”. In: *Bulletin of Alloy Phase Diagrams* 4.4 (1983), pp. 407–410. ISSN: 0197-0216. DOI: `10.1007/BF02868094`. URL: `https://doi.org/10.1007/BF02868094`.

[43] Shen Qiu et al. “Manipulating Adsorption–Insertion Mechanisms in Nanostructured Carbon Materials for High-Efficiency Sodium Ion Storage”. In: *Advanced Energy Materials* 7.17 (Sept. 2017), pp. 1–11. ISSN: 16146840. DOI: `10.1002/aenm.201700403`. URL: `http://doi.wiley.com/10.1002/aenm.201700403`.

[44] Yang Wen et al. “Expanded graphite as superior anode for sodium-ion batteries”. In: *Nature Communications* 5.May (2014), pp. 1–10. ISSN: 20411723. DOI: `10.1038/ncomms5033`.

[45] Yihang Liu et al. “Red Phosphorus Nanodots on Reduced Graphene Oxide as a Flexible and Ultra-Fast Anode for Sodium-Ion Batteries”. In: *ACS Nano* 11.6 (2017), pp. 5530–5537. ISSN: 1936086X. DOI: `10.1021/acsnano.7b00557`.

[46] Pin Liu et al. “A waste biomass derived hard carbon as a high-performance anode material for sodium-ion batteries”. In: *J. Mater. Chem. A* 4 (34 2016), pp. 13046–13052. DOI: `10.1039/C6TA04877C`. URL: `http://dx.doi.org/10.1039/C6TA04877C`.

[47] Huan Liu et al. “Creative utilization of natural nanocomposites: nitrogen-rich mesoporous carbon for a high-performance sodium ion battery”. In: *J. Mater. Chem. A* 5 (20 2017), pp. 9572–9579. DOI: `10.1039/C7TA01891F`. URL: `http://dx.doi.org/10.1039/C7TA01891F`.

[48] Ning Sun et al. “Facile synthesis of free-standing, flexible hard carbon anode for high-performance sodium ion batteries using graphene as a multi-functional binder”. In: *Carbon* 137 (2018), pp. 475–483. ISSN: 00086223. DOI: `10.1016/j.carbon.2018.05.056`. URL: `https://doi.org/10.1016/j.carbon.2018.05.056`.

[49] Suqing Wang et al. “Free-Standing Nitrogen-Doped Carbon Nanofiber Films: Integrated Electrodes for Sodium-Ion Batteries with Ultralong Cycle Life and Superior Rate Capability”. In: *Advanced Energy Materials* 6.7 (2016). ISSN: 16146840. DOI: `10.1002/aenm.201502217`.

[50] Huan Liu et al. “3D-0D Graphene-Fe3O4 Quantum Dot Hybrids as High-Performance Anode Materials for Sodium-Ion Batteries”. In: *ACS Applied Materials and Interfaces* 8.40 (2016), pp. 26878–26885. ISSN: 19448252. DOI: `10.1021/acsami.6b09496`.

[51] Hanna He et al. “Plasma-Induced Amorphous Shell and Deep Cation-Site S Doping Endow TiO2 with Extraordinary Sodium Storage Performance”. In: *Advanced Materials* 30.26 (2018). ISSN: 15214095. DOI: `10.1002/adma.201801013`.

[52] Hai Yang et al. “MoS2 embedded in 3D interconnected carbon nanofiber film as a free-standing anode for sodium-ion batteries”. In: *Nano Research* 11.7 (2018), pp. 3844–3853. ISSN: 19980000. DOI: `10.1007/s12274-017-1958-8`.

[53] Yujie Zhu et al. “Red phosphorus-single-walled carbon nanotube composite as a superior anode for sodium ion batteries”. In: *ACS Nano* 9.3 (2015), pp. 3254–3264. ISSN: 1936086X. DOI: `10.1021/acsnano.5b00376`.

[54] Mouad Dahbi et al. “High performance red phosphorus electrode in ionic liquid-based electrolyte for Na-ion batteries”. In: *Journal of Power Sources* 363 (2017), pp. 404–412. ISSN: 03787753. DOI: `10.1016/j.jpowsour.2017.07.089`. URL: `http://dx.doi.org/10.1016/j.jpowsour.2017.07.089`.

[55] Peng Ge et al. “Rodlike Sb2Se3 Wrapped with Carbon: The Exploring of Electrochemical Properties in Sodium-Ion Batteries”. In: *ACS Applied Materials and Interfaces* 9.40 (2017), pp. 34979–34989. ISSN: 19448252. DOI: `10.1021/acsami.7b10886`.

[56] Chunjuan Tang et al. “ZnSe Microsphere/Multiwalled Carbon Nanotube Composites as High-Rate and Long-Life Anodes for Sodium-Ion Batteries”. In: *ACS Applied Materials and Interfaces* 10.23 (2018), pp. 19626–19632. ISSN: 19448252. DOI: `10.1021/acsami.8b02819`.

[57] R. E. Franklin. “Crystallite Growth in Graphitizing and Non-Graphitizing Carbons”. In: *Proceedings of the Royal Society A: Mathematical, Physical and Engineering Sciences* 209.1097 (Oct. 1951), pp. 196–218. ISSN: 1364-5021. DOI: `10.1098/rspa.1951.0197`. URL: `http://rspa.royalsocietypublishing.org/cgi/doi/10.1098/rspa.1951.0197`.

[58] B. E. Warren. “X-Ray Diffraction Study of Carbon Black”. In: *The Journal of Chemical Physics* 2.9 (1934), pp. 551–555. DOI: `10.1063/1.1749528`. URL: `https://doi.org/10.1063/1.1749528`.

[59] Pascal Ge and Mireille Fouletier. “Electrochemical intercalation of sodium in graphite”. In: *Solid State Ionics* 28-30 (1988), pp. 1172–1175. ISSN: 0167-2738. DOI: `https://doi.org/10.1016/0167-2738(88)90351-7`. URL: `https://www.sciencedirect.com/science/article/pii/0167273888903517`.

[60] Adrian Beda et al. “Hard carbon key properties allow for the achievement of high Coulombic efficiency and high volumetric capacity in Na-ion batteries”. In: *Journal of Materials Chemistry A* 9.3 (2021), pp. 1743–1758. ISSN: 20507496. DOI: `10.1039/d0ta07687b`.

[61] Xingbin Yan et al. “Microstructure and mechanical properties of hard carbon films prepared by heat treatment of a polymer on steel substrate”. In: *Surface and Coatings Technology* 190.2-3 (2005), pp. 206–211. ISSN: 02578972. DOI: `10.1016/j.surfcoat.2004.03.002`.

[62] Stevanus Alvin et al. “Revealing sodium ion storage mechanism in hard carbon”. In: *Carbon* 145 (Apr. 2019), pp. 67–81. ISSN: 00086223. DOI: `10.1016/j.carbon.2018.12.112`.

[63] E. Peled. “The Electrochemical Behavior of Alkali and Alkaline Earth Metals in Nonaqueous Battery Systems—The Solid Electrolyte Interphase Model”. In: *Journal of The Electrochemical Society* 126.12 (1979), pp. 2047–2051. ISSN: 0013-4651. DOI: `10.1149/1.2128859`.

[64] Satu Kristiina Heiskanen, Jongjung Kim, and Brett L. Lucht. “Generation and Evolution of the Solid Electrolyte Interphase of Lithium-Ion Batteries”. In: *Joule* 3.10 (2019), pp. 2322–2333. ISSN: 2542-4351. DOI: `https://doi.org/10.1016/j.joule.2019.08.018`. URL: `https://www.sciencedirect.com/science/article/pii/S2542435119304210`.

[65] Gebrekidan Gebresilassie Eshetu et al. “Impact of the electrolyte salt anion on the solid electrolyte interphase formation in sodium ion batteries”. In: *Nano Energy* 55 (Jan. 2019), pp. 327–340. ISSN: 22112855. DOI: `10.1016/j.nanoen.2018.10.040`.

[66] D. A. Stevens and J. R. Dahn. “An In Situ Small-Angle X-Ray Scattering Study of Sodium Insertion into a Nanoporous Carbon Anode Material within an Operating Electrochemical Cell”. In: *J. Electrochem. Soc.* 147.12 (Dec. 2000), pp. 4428–4431. ISSN: 00134651. DOI: `10.1149/1.1394081`. URL: `http://jes.ecsdl.org/cgi/doi/10.1149/1.1394081`.

[67] D. A. Stevens and J. R. Dahn. “High Capacity Anode Materials for Rechargeable Sodium-Ion Batteries”. In: *Journal of The Electrochemical Society* 147.4 (2000), p. 1271. ISSN: 00134651. DOI: `10.1149/1.1393348`.

[68] D. A. Stevens and J. R. Dahn. “The Mechanisms of Lithium and Sodium Insertion in Carbon Materials”. In: *J. Electrochem. Soc.* 148.8 (Aug. 2001), A803–A811. ISSN: 00134651. DOI: `10.1149/1.1379565`. URL: `http://jes.ecsdl.org/cgi/doi/10.1149/1.1379565`.

[69] Biao Zhang et al. “Correlation between Microstructure and Na Storage Behavior in Hard Carbon”. en. In: *Advanced Energy Materials* 6.1 (Jan. 2016), pp. 1–9. ISSN: 16146840. DOI: `10.1002/aenm.201501588`. URL: `http://`

onlinelibrary.wiley.com/doi/10.1002/aenm.201501588/abstract%20http://onlinelibrary.wiley.com/store/10.1002/aenm.201501588/asset/aenm201501588.pdf?v=1%7B%5C&%7Dt=jeiv7rfa%7B%5C&%7Ds=c089df4d20b144d78ec4d415c984ee59b933932e.

[70] Panxing Bai et al. "Elucidation of the Sodium-Storage Mechanism in Hard Carbons". In: *Advanced Energy Materials* 8.15 (May 2018), pp. 1–9. ISSN: 16146840. DOI: 10.1002/aenm.201703217. URL: http://doi.wiley.com/10.1002/aenm.201703217.

[71] Hongshuai Hou et al. "Carbon Anode Materials for Advanced Sodium-Ion Batteries". In: *Advanced Energy Materials* 7.24 (2017). ISSN: 16146840. DOI: 10.1002/aenm.201602898.

[72] Yuliang Cao et al. "Sodium Ion Insertion in Hollow Carbon Nanowires for Battery Applications". In: *Nano Letters* 12.7 (July 2012), pp. 3783–3787. ISSN: 1530-6984. DOI: 10.1021/nl3016957. URL: http://pubs.acs.org/doi/10.1021/nl3016957.

[73] Jia Ding et al. "Carbon nanosheet frameworks derived from peat moss as high performance sodium ion battery anodes". In: *ACS Nano* 7.12 (2013), pp. 11004–11015. ISSN: 19360851. DOI: 10.1021/nn404640c.

[74] Elmira Memarzadeh Lotfabad et al. "Origin of non-SEI related coulombic efficiency loss in carbons tested against Na and Li". In: *J. Mater. Chem. A* 2 (46 2014), pp. 19685–19695. DOI: 10.1039/C4TA04995K. URL: http://dx.doi.org/10.1039/C4TA04995K.

[75] Joshua M. Stratford et al. "Correlating Local Structure and Sodium Storage in Hard Carbon Anodes: Insights from Pair Distribution Function Analysis and Solid-State NMR". In: *Journal of the American Chemical Society* 143.35 (2021), pp. 14274–14286. ISSN: 15205126. DOI: 10.1021/jacs.1c06058.

[76] Kudakwashe Chayambuka et al. "An experimental and modeling study of sodium-ion battery electrolytes". In: *Journal of Power Sources* 516.October (2021), p. 230658. ISSN: 03787753. DOI: 10.1016/j.jpowsour.2021.230658. URL: https://doi.org/10.1016/j.jpowsour.2021.230658.

[77] Gregory L. Plett. *Battery Management systems.* London, UK, Artech House, 2015. ISBN: 9781630810276.

[78] Hui Chen et al. "Review and perspective: Sapphire optical fiber cladding development for harsh environment sensing". In: *Applied Physics Reviews* 5.1 (2018). ISSN: 19319401. DOI: 10.1063/1.5010184. URL: http://dx.doi.org/10.1063/1.5010184.

[79] Albert Einstein and Leopold Infeld. *The evolution of physics: From early concepts to relativity and quanta.* New York, Simon and Schuster, 1938, 1938, p. 306. ISBN: 9780671201562. URL: http://books.simonandschuster.com/Evolution-of-Physics/Albert-Einstein/9780671201562/browse_inside.

[80] Donald R. Huffman Craig F. Bohren. *Absorption and Scattering of Light by Small Particles.* Berlin, Wiley-VCH Verlag GmbH, 2010. ISBN: 9780471293408.

[81] Elin M. Larsson et al. "Nanoplasmonic sensing for nanomaterials science". In: *Nanophotonics* 1.3-4 (2012), pp. 249–266. ISSN: 21928606. DOI: 10.1515/nanoph-2012-0029.

[82] FHR. *Sputtering technology.* https://www.fhr.biz/en/thin-film-technology/sputtering-technology/. Accessed: 2021-11-10. 2021.

[83] Scott C. Warren, David A. Walker, and Bartosz A. Grzybowski. "Plasmoelectronics: Coupling plasmonic excitation with electron flow". In: *Langmuir* 28.24 (2012), pp. 9093–9102. ISSN: 07437463. DOI: `10.1021/la300377j`.

[84] Jiangong Zhu et al. "Investigation of lithium-ion battery degradation mechanisms by combining differential voltage analysis and alternating current impedance". In: *Journal of Power Sources* 448 (2020), p. 227575. ISSN: 0378-7753. DOI: `https://doi.org/10.1016/j.jpowsour.2019.227575`. URL: `https://www.sciencedirect.com/science/article/pii/%20%5C%5C%20S037877531931568X`.

[85] Mikhail Polyanskiy. *Refractive index database.* https://refractiveindex.info/?shelf=main&book=H2O&page=Hale. Accessed: 2021-12-20. 2021.

[86] MATLAB. *version 9.10.0.1649659 (R2021a) Update 1.* Natick, Massachusetts: The MathWorks Inc., 2021.

[87] Yibin Bu, J. W.Hans Niemantsverdriet, and Hans O.A. Fredriksson. "Cu Model Catalyst Dynamics and CO Oxidation Kinetics Studied by Simultaneous in Situ UV-Vis and Mass Spectroscopy". In: *ACS Catalysis* 6.5 (2016), pp. 2867–2876. ISSN: 21555435. DOI: `10.1021/acscatal.5b02861`.

A

Appendix 1

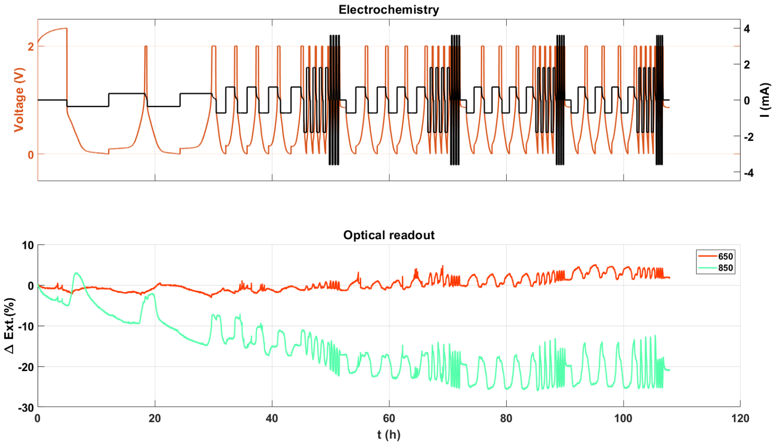

Figure A.1: An overview of the different parameters measured during *operando* measurements for cell 2. 650 and 850 nm were chosen as representative wavelengths according to figure 4.10

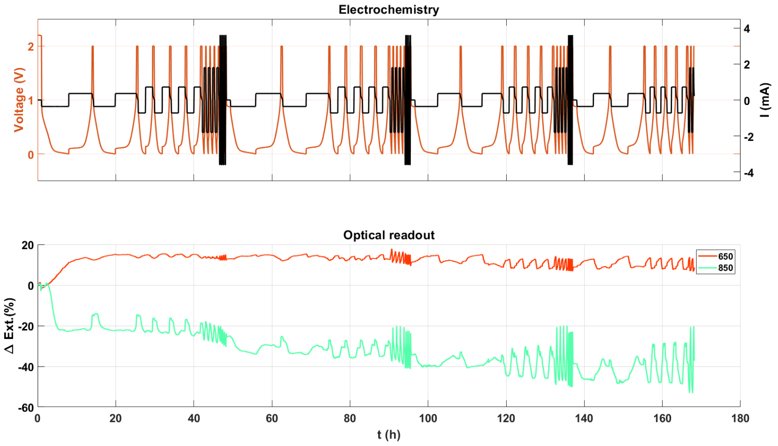

Figure A.2: An overview of the different parameters measured during *operando* measurements for cell 3. 650 and 850 nm were chosen as representative wavelengths according to figure 4.10

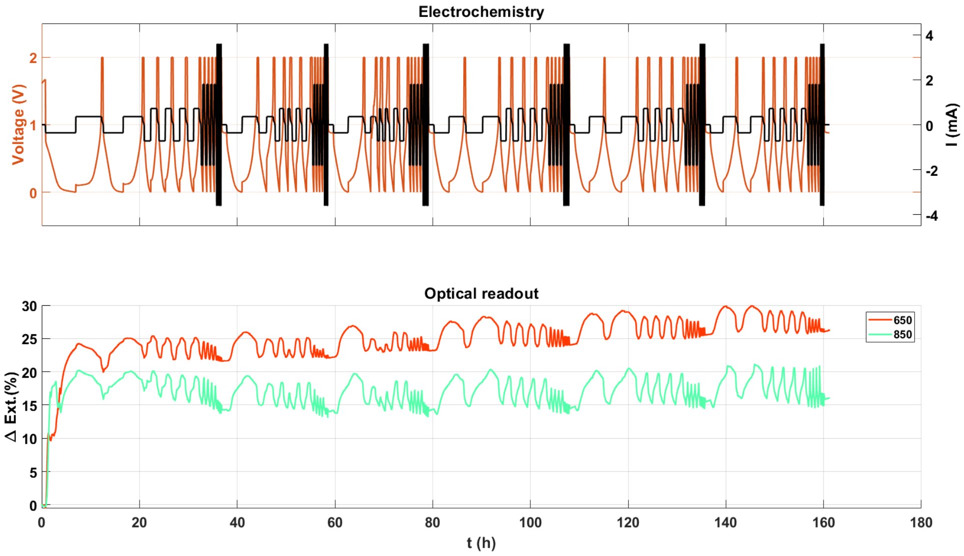

Figure A.3: An overview of the different parameters measured during *operando* measurements for cell 5. 650 and 850 nm were chosen as representative wavelengths according to figure 4.10

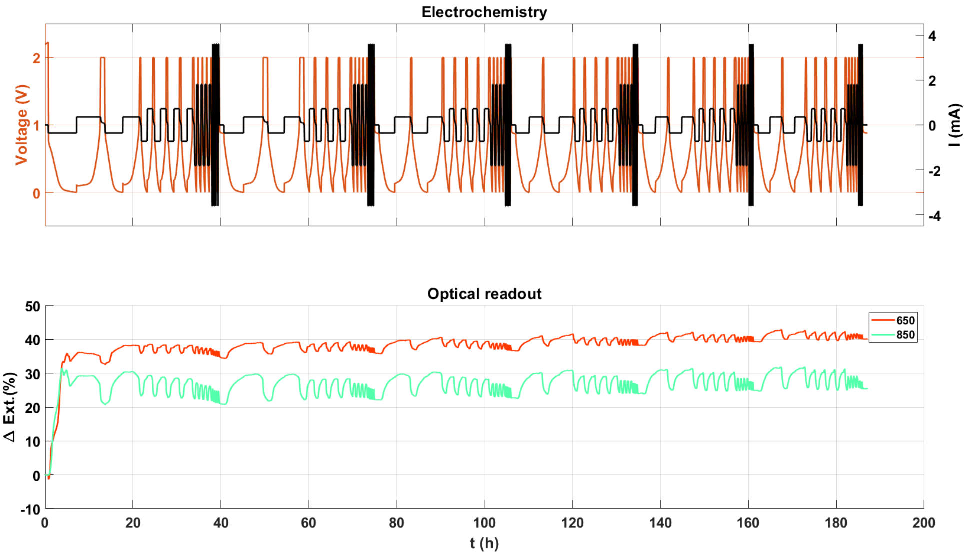

Figure A.4: An overview of the different parameters measured during *operando* measurements for cell 6. 650 and 850 nm were chosen as representative wavelengths according to figure 4.10

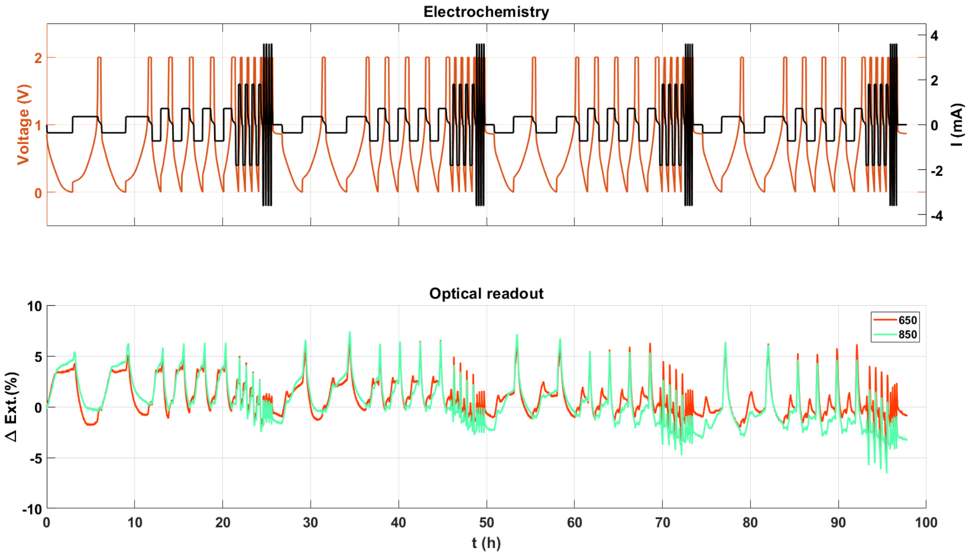

Figure A.5: An overview of the different parameters measured during *operando* measurements for cell 8. 650 and 850 nm were chosen as representative wavelengths according to figure 4.10

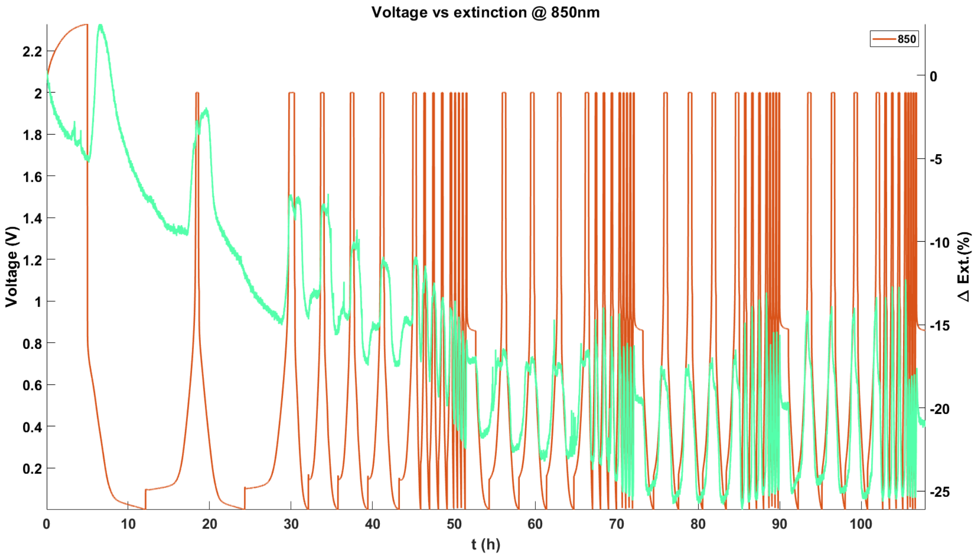

Figure A.6: Voltage signal and Δextinction vs time for cell 2.

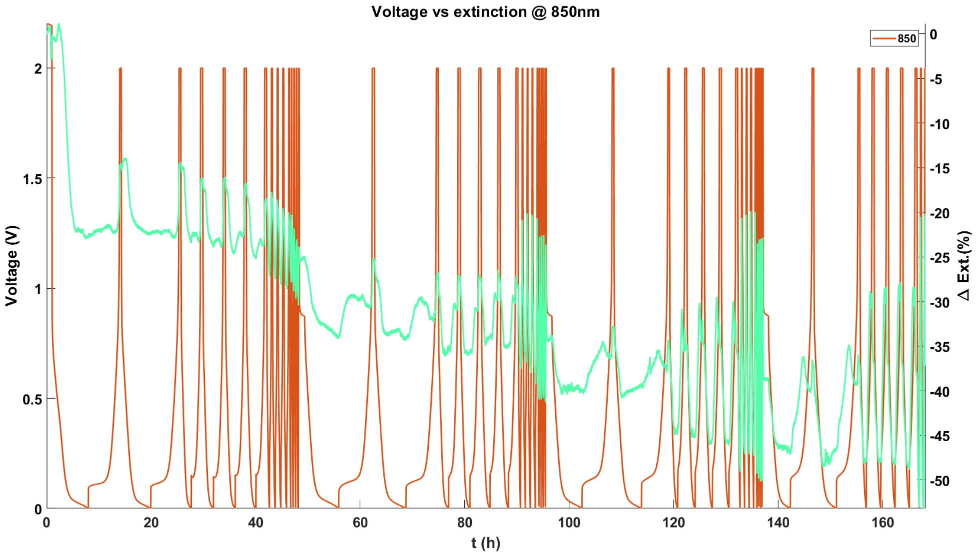

Figure A.7: Voltage signal and Δextinction vs time for cell 3.

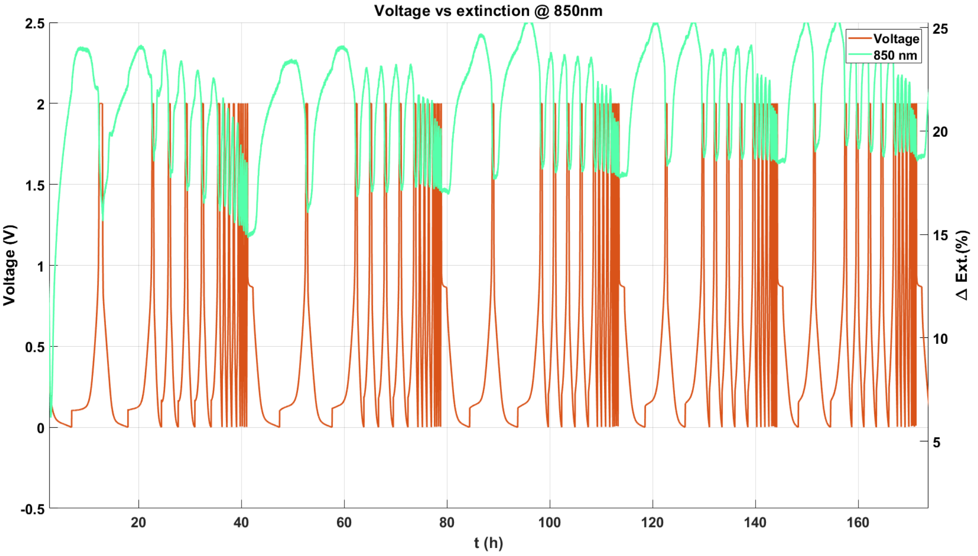

Figure A.8: Voltage signal and Δextinction vs time for cell 4.

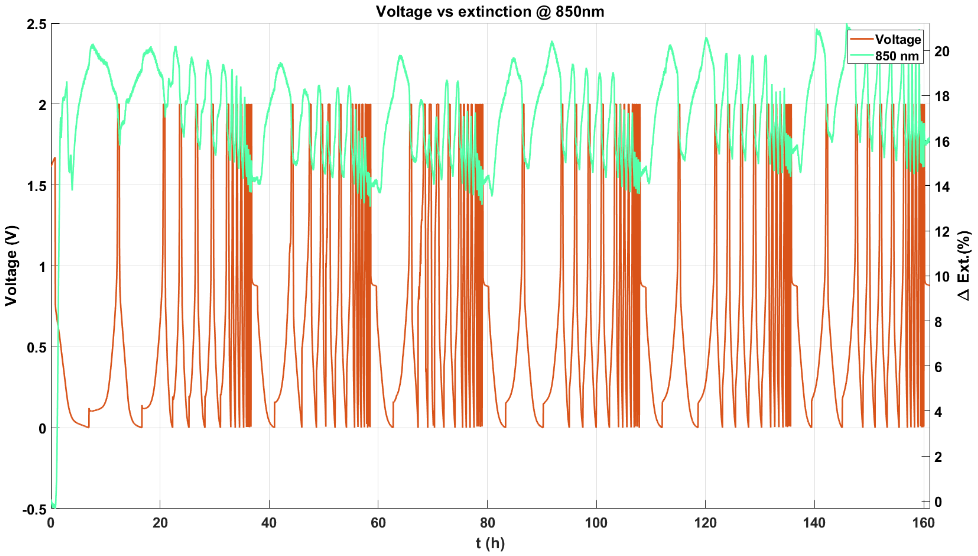

Figure A.9: Voltage signal and Δextinction vs time for cell 5.

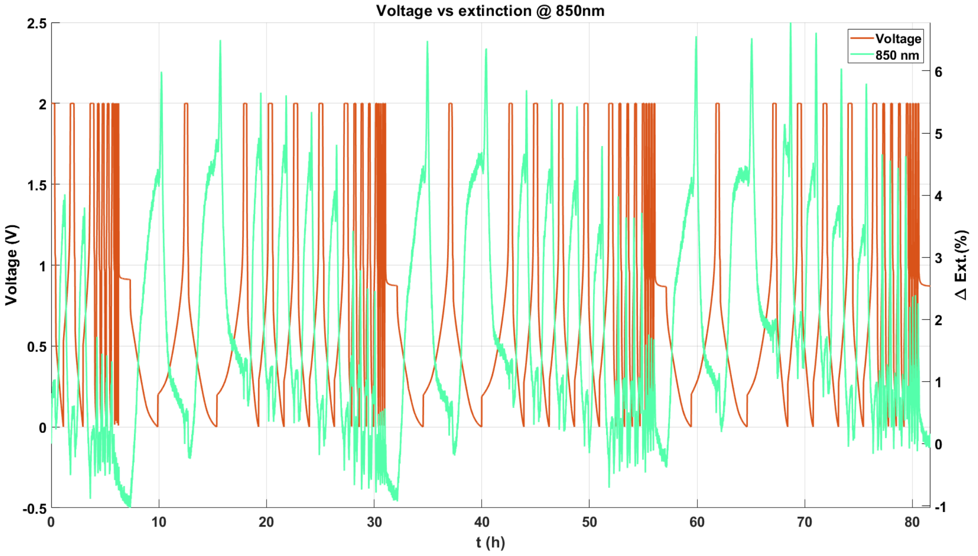

Figure A.10: Voltage signal and Δextinction vs time for cell 7.

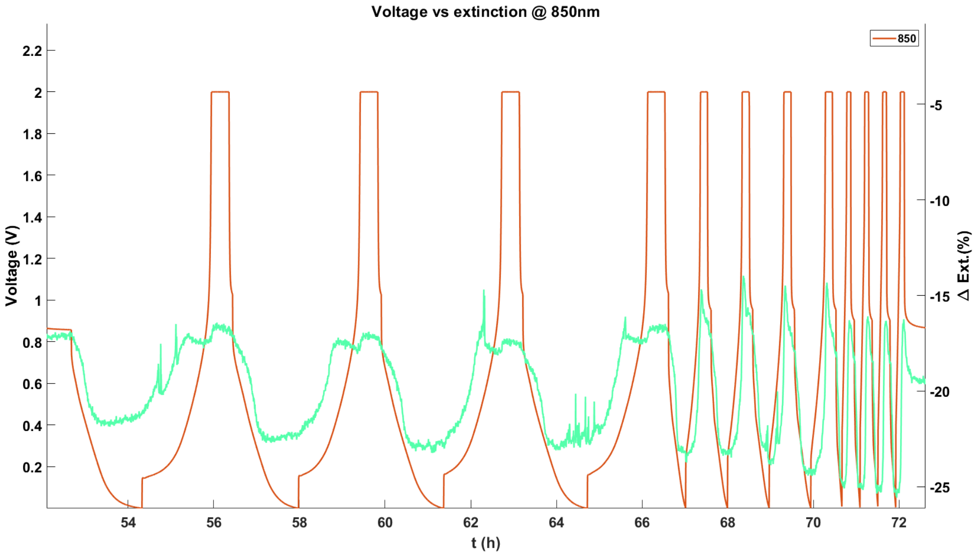

Figure A.11: Voltage signal and Δextinction vs time for cell 2.

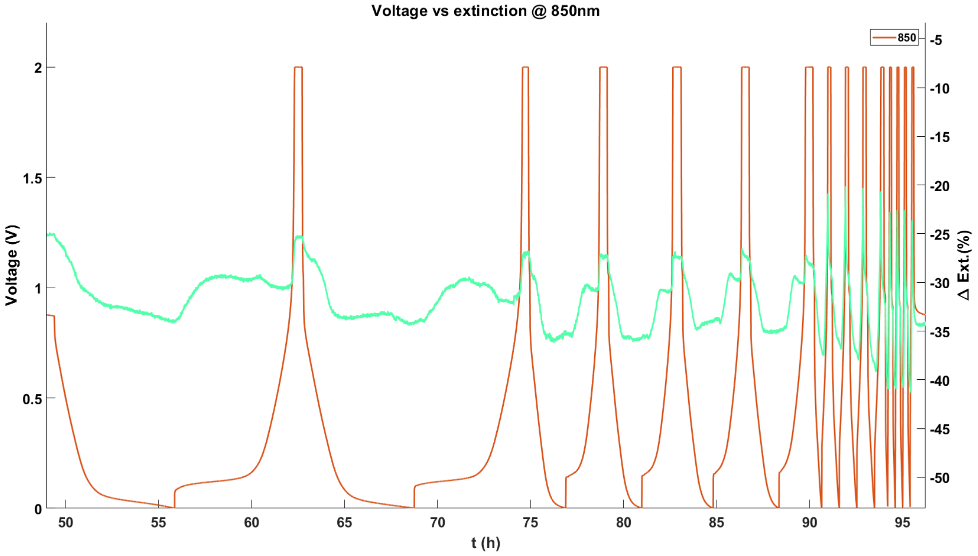

Figure A.12: Voltage signal and Δextinction vs time for cell 3.

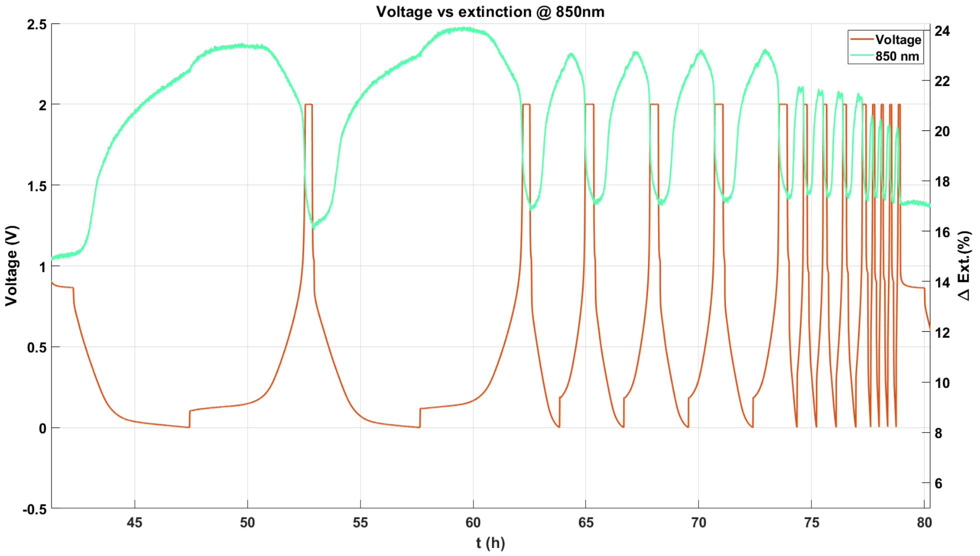

Figure A.13: Voltage signal and Δextinction vs time for cell 4.

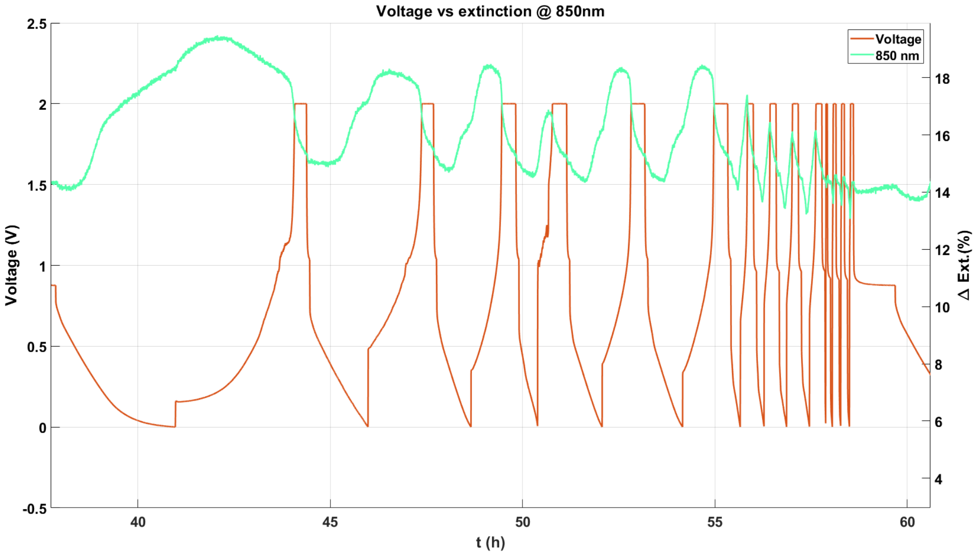

Figure A.14: Voltage signal and Δextinction vs time for cell 5.

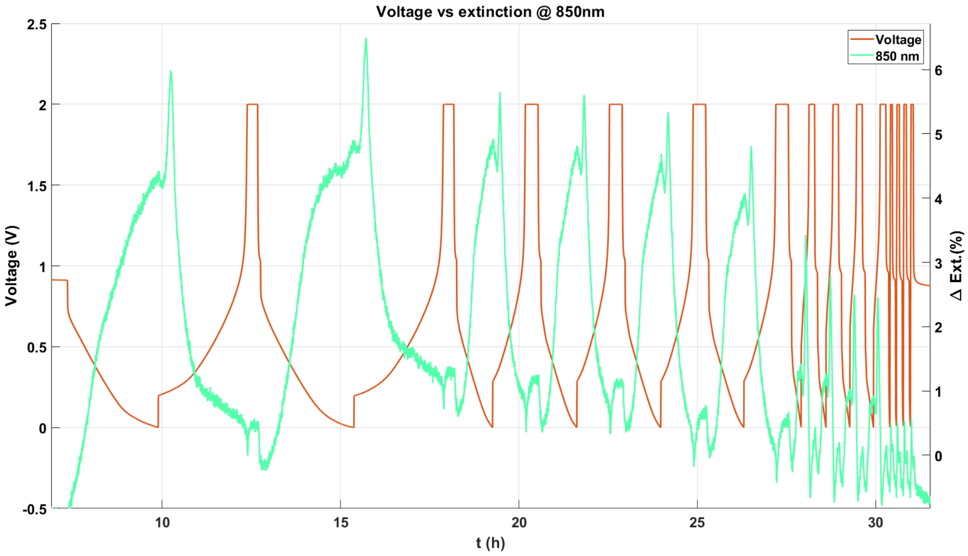

Figure A.15: Voltage signal and Δextinction vs time for cell 7.

DEPARTMENT OF PHYSICS
CHALMERS UNIVERSITY OF TECHNOLOGY
Gothenburg, Sweden
www.chalmers.se

CHALMERS
UNIVERSITY OF TECHNOLOGY